water

MDPI

Article

Characteristics of Accelerations and Pressure Gradient during Run-Down of Solitary Wave over Very Steep Beach: A Case Study

Chang Lin [1], Wei-Ying Wong [1,*], Rajkumar V. Raikar [2], Hwung-Hweng Hwung [3] and Ching-Piao Tsai [1]

[1] Department of Civil Engineering, National Chung Hsing University, Taichung City 40227, Taiwan; chenglin@nchu.edu.tw (C.L.); cptsai@nchu.edu.tw (C.-P.T.)
[2] Department of Civil Engineering, KLE Dr. M. S. Sheshgiri College of Engineering and Technology, Angol Main Road, Udyambag, Belgaum, Karnataka 590008, India; rvraikar@klescet.ac.in
[3] International Wave Dynamics Research Center, National Cheng Kung University, Tainan City 701, Taiwan; hhhwung@mail.ncku.edu.tw
* Correspondence: wongweiying25@gmail.com; Tel.: +886-4-285-3941

Received: 22 January 2019; Accepted: 7 March 2019; Published: 13 March 2019

Abstract: An experimental investigation is performed to elucidate the variations of accelerations and pressure gradients in the external stream of retreating flow during the run-down phase of a non-breaking solitary wave, propagating over a 1:3 sloping beach. Two solitary waves that have the incident wave heights (H_0) of 2.9 and 5.8 cm, with respective still water depths (h_0) of 8.0 and 16.0 cm (Cases A and B), were generated in a wave flume, resulting in the incident wave-height to water-depth ratios (H_0/h_0) being identically equal to 0.363. The latter case was only used to highlight the non-dimensional features of the wave celerity, the time history of horizontal velocity and the breaker type, which all exhibit similarity to those of the former. Two flow visualization techniques such as particle trajectory method and fluorescent dye strip and a high-speed particle image velocimetry (HSPIV) were utilized to provide the flow images and velocity fields. Based on the ensemble-averaged velocity fields and profiles, the partially depth-averaged (i.e., excluding the part in the boundary layer) values of accelerations and pressure gradient at a specified measuring section are then smoothed by a symmetric five-point smoothing scheme. Eventually, the smoothed values of the accelerations and pressure gradient are used to highlight the dynamic features of the external stream of retreating flow. It is found that, at the section of the incipient flow separation, the non-dimensional local acceleration (with respect to the gravity acceleration) in the offshore direction keeps increasing from the moment at which the run-up motion ends to the counterpart at which the incipient flow separation occurs. Afterwards, growth of the primary vortex develops with its core translating offshore. The corresponding non-dimensional local acceleration at the (moving) core section increases to a maximum of around 1.0 at the instant for occurrence of the hydraulic jump with abrupt rise of the free surface; and then decreases to zero at time for transformation of the curling jet into the projecting jet. The results exhibit that the external stream of retreating flow is accelerated temporally in the offshore direction for the interval between the time for the end of run-up motion and that for the formation of projecting jet. However, for later time interval up to generation of the two-phase flow field, the non-dimensional local acceleration in the offshore direction varies from zero to a negative maximum of −2.117 at the moment for the projecting jet heading downward before the impingement. It then decreases in magnitude continuously. The trend reveals that the external stream is decelerated temporally in the offshore direction for this later time interval. Further, at the section of the incipient flow separation, the non-dimensional pressure gradient (also with reference to the gravity acceleration) in the offshore direction increases from 0.225 for the time at which the run-up motion ends to 0.721 for the instant at which the incipient flow separation takes place. The trend highlights the external stream being under increasing adverse

pressure gradient and more decelerated spatially with the increasing time, thus resulting in occurrence of the incipient flow separation. Afterwards, the value of the non-dimensional pressure gradient keeps increasing and eventually reaches a positive maximum of 2.011 and then decreases consecutively until the two-phase flow field is generated. In addition, due to the influence of acceleration of the external stream in the offshore direction, the non-dimensional vorticity of primary vortex core increases with increasing time up to the moment for occurrence of the projecting jet. Nevertheless, the non-dimensional vorticity of primary vortex core keeps decreasing with increasing time T for the later time interval due to the influence of deceleration of the external stream in the offshore direction. Finally, considerably large magnitudes of the non-dimensional accelerations and pressure gradient greater than 1.5 taking place at two non-dimensional times are worthy of noting. The negative maximum value of the non-dimensional convective acceleration equal to −2.005 appears at the instant for the occurrence of hydraulic jump. In addition, the negative maximum values of the non-dimensional local acceleration, total acceleration and pressure gradient unexpectedly as high as −2.117, −1.694 and 2.011, respectively, appear simultaneously at time for the projecting jet heading towards the retreating free surface. Under such a situation, the external stream of retreating flow is highly decelerated in the offshore direction under the fairly large adverse pressure gradient, thus forcing the retreating flow to move upwards rapidly. Meanwhile, the non-dimensional local acceleration in the vertical direction is surprisingly found to be 3.37. The result strongly reconfirms the evident rise of the free surface in the vicinity of the core section and reveals very rapid change from negative, via nearly zero, to positive vertical velocity.

Keywords: solitary wave; run-down process; retreating flow; external stream, boundary layer flow; swash front; acceleration; pressure gradient; vortex structure

1. Introduction

Solitary wave, which is one of long waves, propagating over a sloping beach is characterized by the run-up motion up to the instant when it ends with the maximum run-up height being reached; and by the run-down counterpart while it starts soon after the end of run-up motion. Related studies on the features of run-up and run-down motions of the solitary wave can evidently enhance understanding of the physical problem of long-wave hydrodynamics associated with the shoreward inundation of a tsunami-like flow and the offshore transport of a retreated flow.

This study is an extension of Lin et al. [1], aiming to elucidate the dynamic characteristics of acceleration and pressure gradient of the external stream in the retreating flow during run-down process of the solitary wave (with $H_0/h_0 = 0.363$) traveling on the 1:3 sloping beach. For completeness, previous literatures (Lin et al. [1]) are briefly surveyed in the following.

A series of theoretical and numerical models have been used to investigate the spatio-temporal variation of free surface elevation/profile, breaker type, mass transport, maximum run-up height and even velocity fields/profiles of distinct waves traveling over sloping beaches. For example, the approximate linear and nonlinear theories (Carrier and Greenspan [2]; Synolakis [3]), the numerical model employing the Lax-Wendroff method (Kobayashi et al. [4]), the Lagrangian finite-element Boussinesq wave model (Zelt [5]), the completely nonlinear wave model (Grilli et al. [6,7]), the model based on RANS equations and improved k-ε equations (Lin and Liu [8], Lin et al. [9]), the approximate mathematical model using a double power series of two small parameters in the Navier-Stokes equation and the boundary layer conditions (Scandura et al. [10]) and a modified edition of the open source code—OpenFOAM® (Higuera et al. [11], https://github.com/phicau/olaFlow)—were all tested and reported.

On the other hand, the experimental results of spatio-temporal variation in the velocity fields/profiles using PIV (Particle Image Velocimetry) or HSPIV (High-speed PIV) have been presented for solitary waves propagating over sloping beaches with different slopes in the nearshore zone (including the shoaling, surf and/or swash zone). Representative examples include Lin et al. [9] for waves traveling on a sloping plane beach with the slope S_0 = 1:1.732, Jensen et al. [12] for S_0 =

1:5.38, Pedersen et al. [13] for S_0 = 1:5.67, Lin et al. [14,15] for S_0 = 1:10 and 1:5, Smith et al. [16] for S_0 = 1:11.2 and Lin et al. [1] for S_0 = 1:3. Note that evolution of the separated shear layer (stemming from the instability at the surface of sloping beach), accompanied by development of the topological vortex structure, was subsequently elucidated by Lin et al. [1,14,15] during run-down phase of solitary wave. More recently, Petrotta et al. [17] employed a Vectrino Profiler to measure the velocity profiles beyond a sandy bed with migrating ripple bedforms, which were generated under both regular and random waves, traveling over a 1:10 sloping beach.

As indicated by Jensen et al. [12], obtaining accelerations is more difficult than velocities due to very fast temporal and spatial fluctuations even in the fine calculation of numerical model or precise PIV/HSPIV measurements. Direct measurements of acceleration and pressure gradient in the wave-induced flow field using intrusive measuring devices are almost impossible due to the severe interference effect (except those installed flush on the surface of a rigid boundary). Instead, the non-intrusive, image-based measurement technique, like PIV or HSPIV with high sampling rate and pixel resolution, can be employed to precisely obtain the velocity fields. Then, based on the incompressible Navier-Stokes equation of motion, the spatio-temporal variations of local and convective accelerations as well as the pressure gradient can be calculated accordingly. Even rapid development of the high-resolved numerical model/PIV (or HSPIV) measurements with high temporal and spatial resolutions has come true currently, however, related numerical/experimental studies on the features of acceleration and pressure gradient in the wave-induced flow field are fairly few.

Chang and Liu [18] used the traditional PIV system (with a sampling rate of 1 Hz) to measure the velocity and acceleration of overturning jet of a plunging breaker for the periodic wave (with a wave-amplitude/period of 7.0 cm/1.0 s), propagating over a constant water depth of 20.0 cm. Their findings showed that the fluid particle acceleration had a maximum value of 1079.1 cm/s^2 (=1.1g, with g being the gravity acceleration) while the overturning jet right touching the water surface. Utilizing an extended PIV system with two cameras (focusing on an identical field of view (FOV) but recording at different time instants), Jensen et al. [19] measured the instantaneous velocity fields/profiles and then computed the local acceleration fields/profiles of periodic waves propagating over horizontal bottom with a constant water depth of 60.0 cm. For the monochromatic waves with wave-period of 0.702/1.667 s and wave-amplitude of 1.09–2.05/7.50 cm, the acceleration right on the wave free surface were 96–160 cm/s^2 (=0.098g–0.163g). In addition, Jensen et al. [12] used a highly-sensitive PIV system to measure the velocity field and analyzed the local acceleration field of solitary waves (with H_0/h_0 = 0.120–0.663) traveling on a 1:5.38 sloping beach near the still-water shoreline. Their result surprisingly reported that a maximum (nearly horizontal) acceleration of about 2.0g took place behind the toe of almost vertical front of the wave profile for a strongly nonlinear solitary wave (H_0/h_0 = 0.663). Employing the volume-of-fluid Navier-Stokes solver coupled with k-ε turbulence closure model, Puleo et al. [20] presented numerically the fluid particle accelerations of periodic waves propagating over sloping beaches with S_0 = 1:12.51, 1:1.49 and 1:2.30 in the swash zone. They predicted that the local acceleration in the onshore direction occurred only near the limit of run-down phase, however, the convective acceleration held the maximum value during the time interval of run-down phase. The maximum magnitudes of acceleration were in the range of ((2–4)g × sinθ) with θ being the inclination angle of the sloping beach.

Deploying an array of ten pressure transducers on the surface of sloping beach, Pedrozo-Acuna et al. [21] presented variations of the pressure field and gradient of periodic plunging waves traveling across the nearshore zone. Their findings showed that the local acceleration could be used to interpret the contribution of pressure gradients in the shoaling and breaking zones but failed in swash zone. Further, for almost the entire swash period, the minimum pressure gradient was ascertained and the local acceleration having negative value just highlighted the prominent offshore motion of waves. Recently, Higuera et al. [11] used the modified edition of OpenFOAM® to elucidate the relationship between the temporal evolution of vortex structure and the counterpart of pressure gradient field under a developing hydraulic jump, which took place during run-down phase of a solitary wave. It was found that the primary mechanism for vortex formation was closely related to the large adverse pressure gradient along the sloping beach during the offshore transportation of retreating flow from

supercritical to subcritical. Consequently, the extreme value of pressure gradient was estimated to be (1.0–1.3)g/−(1.7–2.0)g on the onshore/offshore side of the abrupt rise of the free surface profile of hydraulic jump; and a maximum counterpart of (1.2–2.0)g/−(1.7–2.0)g appeared on the neighboring/further offshore side of impinging zone while the projecting jet was impinging upon the free surface of the retreating flow.

From the above-mentioned review, it is pertinent to note that a complete evolution of the acceleration (including the local, convective and total accelerations) and pressure gradient during the entire run-down stage of solitary wave were not elucidated in the past. In addition, the relationship between the strength of the primary vortex (which translates towards offshore) and the corresponding acceleration at the moving core section has not explored at all till date. Accordingly, the completely unknown or still rudimentary key topics are itemized as follows: (1) features of flow deceleration or acceleration and adverse or favorable pressure gradient at a specified section where the incipient flow separation takes place; (2) variations in accelerations and pressure gradient of the external stream at distinct core sections for the primary vortex moving offshore; and (3) relationship between the vortex-core strength (in terms of vorticity) and the local acceleration of retreated flow beyond the vortex.

The present study, which is an extension of Lin et al. [1], aims to make clear the related mechanisms for the topics mentioned above during run-down phase of a solitary wave (with H_0/h_0 = 0.363) traveling on a very steep beach with S_0 = 1:3. The quantitative measurement data and qualitative flow-visualized images obtained from the HSPIV measurements and flow visualization test, respectively, will be used to illustrate the associated flow features.

2. Experiment Set-Ups and Instrumentations

A glass-bottom and glass-walled wave flume having the dimension of 14.00 m long, 0.25 m wide and 0.50 m deep was used to perform the experiments. A piston-type wave maker driven by a servo-motor was installed at one end of the wave flume. The wave maker could obey the wave-plate trajectory as developed by Goring [22] and produce the satisfactory solitary waves with high repeatability (Lin et al. [1]). The 1:3 sloping beach having an inclination angle of θ = 18.43° was made of an acrylic sheet of 1.5 cm thick and 200.0 cm long. The beach was mounted inside the flume with its toe being located at 900.0 cm from the wave maker (see Figure 1a).

Two Cartesian coordinate systems are used in the present study (see Figure 1b). The origin (0, 0) cm of the first coordinate system (x, y) is located at the toe of the sloping beach with positive x in the horizontal onshore direction and the positive y in the vertical upward direction, measured from the horizontal bottom. Meanwhile, the second coordinate system, (X, Y), has the same origin (0, 0), as the first one but with the positive X directed shoreward along sloping surface and the positive Y normal upward to the beach surface. The relationship between X and x is $X = 1.0541x$. The time is represented by t [the corresponding non-dimensional time $T = t \times (g/h_0)^{1/2}$] with its value t = 0 (also T = 0) at the instant when the crest of the solitary wave is right above the toe of the sloping beach.

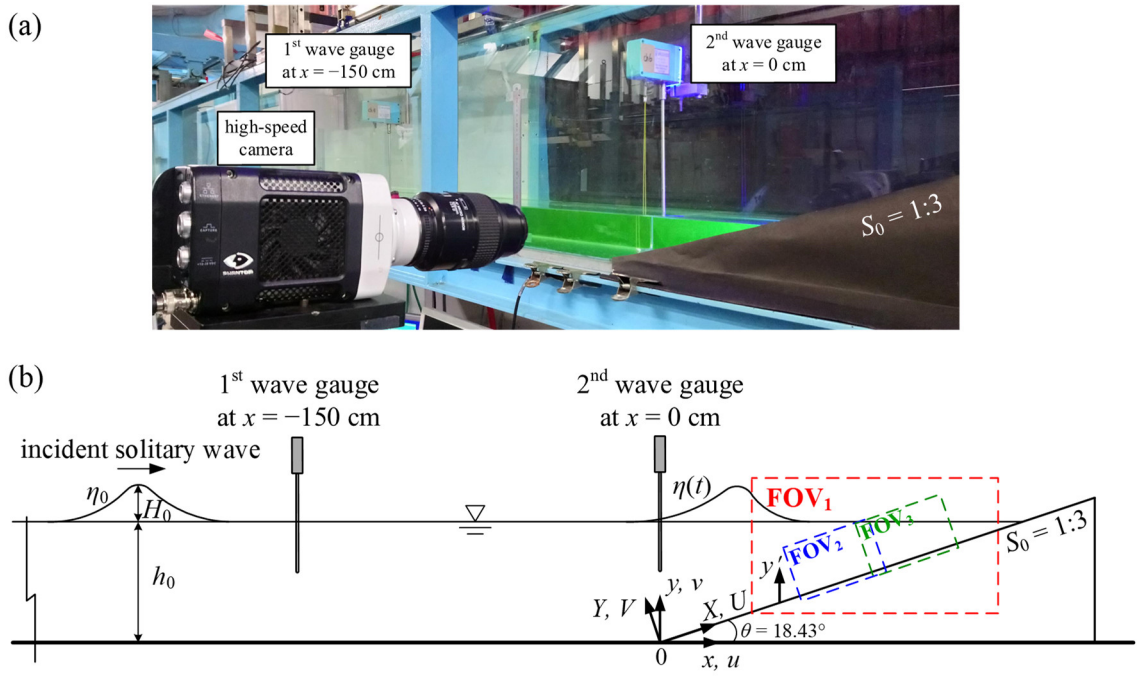

Figure 1. (**a**) A photo showing the wave flume along with the sloping beach, two wave gauges and the high-speed camera; (**b**) Schematic diagram indicating the sloping beach model and two coordinate systems, together with installation of the two wave gauges at x = −150.0 and 0 cm and deployment of three fields of view, FOV_1–FOV_3, for HSPIV measurements.

Two capacitance-type wave gauges, located at x = −150.0 and 0 cm (see Figure 1a,b), were employed to measure the free surface elevations and wave heights. The voltage output of the former/latter was also used as a reference signal to trigger the HSPIV for velocity measurements/a targeted signal to monitor the corresponding time t while the wave crest traveling over the sloping beach.

Two flow visualization techniques (FVT), including particle trajectory method and thin-layered fluorescent dye strip, were utilized to provide the pathline and streakline patterns of flow field underlying the free surface of the solitary wave, respectively. For visualizing the flow field with pathline pattern, titanium dioxide (TiO_2) particles with a mean diameter of 1.8 μm were employed as seeding particles. Further, for the counterpart with streakline pattern, a thin-layered fluorescent dye strip, consisting of a water solution of fluorescein sodium and little salt with a specific gravity of 1.003, was used.

A high-speed digital camera (Phantom M310, Vision Research), which has a maximum framing rate of 3260 Hz under the largest resolution of 1280 × 800 pixel, was employed to capture the spatio-temporal variations of both the free surface profile and the flow field underlying the free surface. A fan-shaped laser light sheet (of 1.5 mm thickness), emitted from a 5W argon-ion laser head (Innova−300, Coherent Inc., Santa Clara, CA, USA), was used to illuminate the motion of the seeding particles or fluorescent dye strip on a vertical plane.

In this study, the velocity measurements were made using the HSPIV system. The system comprised of a high speed digital camera and laser light sheet, which were same as those used in FVT. To investigate the temporal variation of velocity field over the sloping beach for 10.8 cm ≤ x ≤ 20.08 cm, the first field of view (FOV_1, see Figure 1b and Table 1) with a dimension of 9.95 cm wide × 6.22 cm high was employed. On the other hand, for measuring the detailed velocity field close to the sloping beach, two fields of view consisting of FOV_2 and FOV_3 (see Figure 1b and Table 1) having a close-up with 3.50 cm wide × 2.19 cm high were used but with certain overlaps. To ascertain a high time-resolved HSPIV algorithm, the camera was set at a framing rate of 2000 Hz/3000 Hz to take the flow images within FOV_1/(FOV_2 and FOV_3).

Table 1. A list of the range, dimension, pixel resolution and framing rate for each field of view $(FOV)_i$ (i = 1–3).

FOV_i	Range	Dimension	Pixel Resolution	Framing Rate
FOV_1	10.80 cm ≤ x ≤ 20.08 cm	9.95 cm × 6.22 cm	1280 × 800	2000 Hz
FOV_2	13.15 cm ≤ X ≤ 16.65 cm	3.50 cm × 2.19 cm	1280 × 800	3000 Hz
FOV_3	15.75 cm ≤ X ≤ 19.25 cm	3.50 cm × 2.19 cm	1280 × 800	3000 Hz

Two incident solitary waves with the same incident wave-height to water-depth ratio (H_0/h_0) of 0.363 were tested as Case A and Case B. The incident wave heights of the former and latter were H_0 = 2.9 and 5.8 cm and the water depths over the horizontal bottom were h_0 = 8.0 and 16.0 cm, thus resulting in the still water shoreline being located at x = 24.0 and 48.0 cm, respectively. Note that Case B was only used to highlight the non-dimensional features of the wave celerity over horizontal bottom, the time history of horizontal velocity measured at x = 0 cm and the breaker type, which all exhibit similarity to those of Case A. In this study, the HSPIV measurements were repeated for 10 runs. For smoothing the time series of velocities, the ensemble-averaged method was employed. The ensemble-averaged velocity data was then used to describe the spatio-temporal variation of velocity fields and profiles hereafter.

For the details of the experimental set-ups, two FVTs and the deployment of different FOVs for HSPIV, together with the image contrast-enhancement technique and the algorithm for cross correlation analysis of the HSPIV velocity measurements, Lin et al. [1] can be referred. Only a concise edition of the related illustrations is made above. Furthermore, a series of preliminary tests were comprehensively conducted and presented in Lin et al. [1] The tests have confirmed fairly good agreement not only between the free surface elevation measured and that predicted by the theory (Dean and Dalrymple [23]) but also between the velocity fields/profiles measured by HSPIV and those obtained by fiber-optic laser Doppler velocimetry (Ho [24]). Further, the tests also justified the high repeatability of free surface profile and identified the two-dimensionality and laminar flow pattern of boundary layer over the sloping beach.

3. General Description of Run-Up and Run-Down Process of Solitary Wave for Case A

Based on the observations made from continuously recorded images of the free surface profile of solitary wave for Case A, an entire evolution of the solitary wave over the 1:3 sloping beach as shown in Figure 2 can be classified into: (1) Wave crest reaches the toe section located at x = 0 cm for t = 0 s (i.e., T = 0); (2) Wave propagates onshore over the sloping beach with decreasing still water depth and undergoes the subsequent run-up motion (i.e., without wave breaking) for 0 s < t < 0.6545 s (0 < T < 7.25); (3) Wave motion arrives at the maximum run-up height at $x = x_{mrh}$ = 49.04 cm for $t = t_{mrh}$ = 0.6545 s ($T = T_{mrh}$ = 7.25), followed by the tip or contact point of the swash front being nearly fixed at $x = x_{mrh}$ until t = 0.6945 s (to be further stated in Section 6.1.); (4) The (first) run-down motion then occurs during 0.6945 s < t < 1.2130 s (7.69 < T < 13.43). Within this (non-dimensional) time interval, the incipient flow separation (to be addressed later in Section 6.2.) from the beach surface takes place at $x = x_{ifs}$ = 17.84 cm for $t = t_{ifs}$ = 0.9210 s ($T = T_{ifs}$ = 10.20). Soon afterwards, the hydraulic jump with an abrupt rise of the free surface profile (Chow [25]; Subramanya [26]; Sumer et al. [27], to be illustrated in Section 6.3) occurs at $x = x_{hj}$ = 14.8 cm for $t = t_{hj}$ = 1.0068 s ($T = T_{hj}$ = 11.15); and (5) The second run-up starts at t ≥ 1.2130 s (T ≥ 13.43) and then continues the motion up to t = 1.3510 s (T = 14.96).

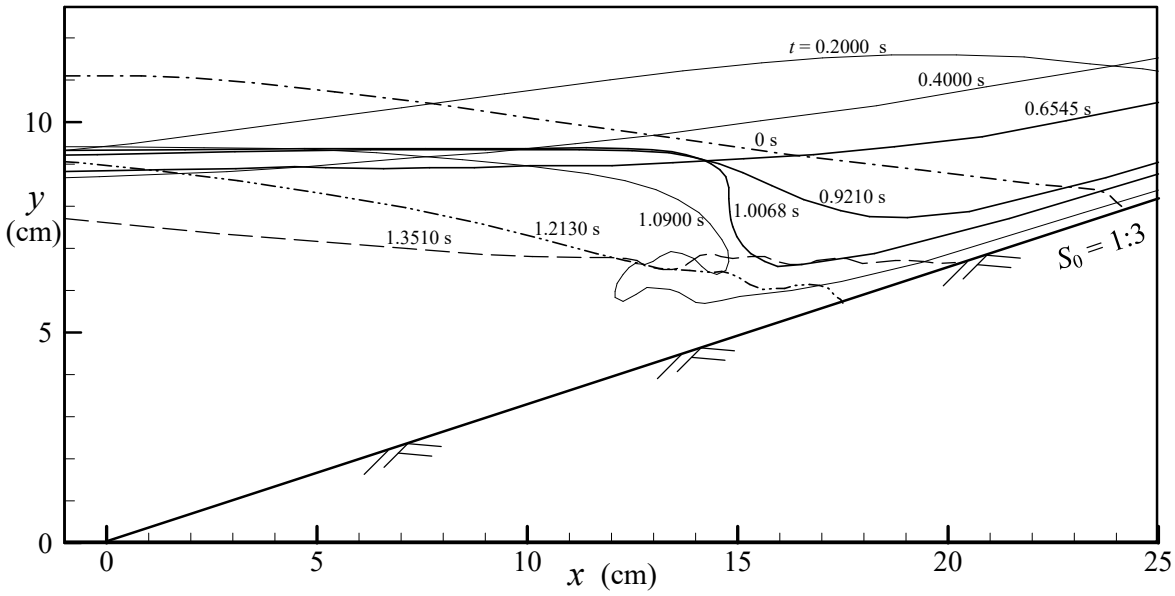

Figure 2. Spatio-temporal variation of the free surface profile for 0 s ≤ t ≤ 1.3510 s (0 ≤ T ≤ 14.96).

4. Justification of Measures Taken to Assure Flow Similarity

As the solitary wave is one of the gravity waves, it is expected that the Froude number similarity (Daily and Harleman [28]; Munson et al. [29]) should exist for various external properties of the wave motion, which is dominated by the gravity force. According to the Froude number similarity for the present Cases A and B, the ratios of the two representative velocity and time scales should be both equal to the square root of the ratio of the two representative length scales for these two different solitary waves (but with the same wave-height to water-depth ratio). Namely,

$$(u_s)_B/(u_s)_A = [(l_s)_B/(l_s)_A]^{1/2}, \quad (1)$$

in which u_s and l_s stand for the representative velocity, time and length scales, respectively.

4.1. Free Surface Elevation/Profile over Horizontal Bottom/Sloping Beach

Figure 3 illustrates a comparison of the time histories of the non-dimensional, 10-run ensemble-averaged free surface elevations, η/h_0, between Case A and Case B measured at x = 0 cm. Note that the results of two individual runs (with runs #1 and #2) of Case A are also shown in Figure 3. It is clearly found that good accordance between both cases exist, exhibiting strong similarity of the non-dimensional free surface elevation η/h_0 versus the non-dimensional time T. Note that the wave height and water depth for Case B (i.e., H_0 = 5.8 cm and h_0 = 16.0 cm) are two times of those for Case A (H_0 = 2.9 cm and h_0 = 8.0 cm). Namely, the ratio of the two length scales is equal to $(l_s)_B/(l_s)_A = (H_0)_B/(H_0)_A = (h_0)_B/(h_0)_A$ = 2.0.

4.2. Wave Celerity Measured over Horizontal Bottom

As proposed by Lin et al. [14], the experimental values of wave celerity over the horizontal bottom, C_0, can be precisely obtained from the cross-correlation analysis for the two time series of free surface elevations measured by two wave gauges with a given separation (e.g., 150.0 cm for the present study). The measured values of C_0 for the present Cases B and A are 144.0 and 102.0 cm/s, respectively. Namely, the ratio of the two wave celerities is $(C_0)_B/(C_0)_A$ = 1.412, nearly equal to 1.414 = $(2)^{1/2} = [(l_s)_B/(l_s)_A]^{1/2} = (u_s)_B/(u_s)_A$ according to Equation (1). This fact does confirm existence of the Froude number similarity for the celerity of solitary wave.

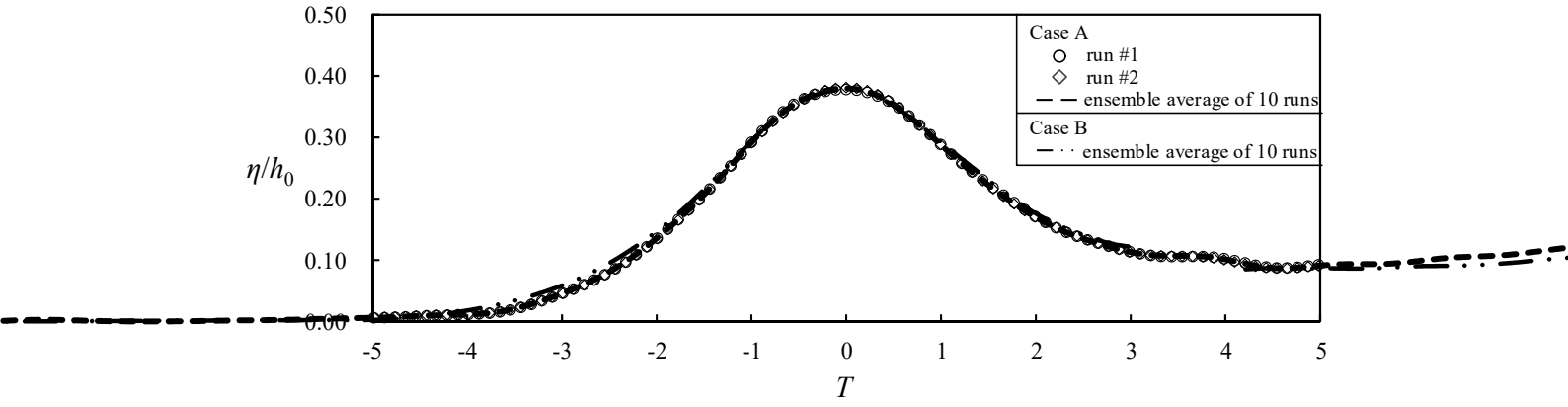

Figure 3. Comparison of the time series of the non-dimensional free surface elevation between Case A and Case B measured at $x = 0$ cm with respect to the non-dimensional time, T.

4.3. Velocity Time Series Obtained at x = 0 cm

Figure 4 shows a comparison of the time histories of the non-dimensional horizontal velocity, u/u_{max}, between the two solitary waves measured at (x/h_0, y/h_0) = (0, 0.94) for Cases A and B. The velocity scale used herein, u_{max}, is defined as the maximum value in the time history of the horizontal velocity with $(u_{max})_A$ = 27.6 cm/s and $(u_{max})_B$ = 38.92 cm/s, respectively. Both data trends are nearly collapsed together although some minute distinctions exist. This evidence supports that the time history of the non-dimensional horizontal velocity for Case A exhibits considerable similarity to that of Case B. Herein, the ratio of the two maximum horizontal velocities, $(u_{max})_B/(u_{max})_A$, is equal to 1.410, very close to $1.414 = (2)^{1/2} = [(l_s)_B/(l_s)_A]^{1/2} = (u_s)_B/(u_s)_A$ according to Equation (3). This result further demonstrates existence of the *Froude number similarity* for the (maximum) horizontal velocity underlying the free surface. Note that, for $3.0 \le T \le 5.0$, the horizontal velocities of both Cases A and B take negative values due to occurrence of flow bifurcation for $T \ge 3.0$ during run-up phase of the solitary wave. Namely, one stream moves onshore and the other transports offshore with flow demarcation curve (Lin et al. [15]) in between.

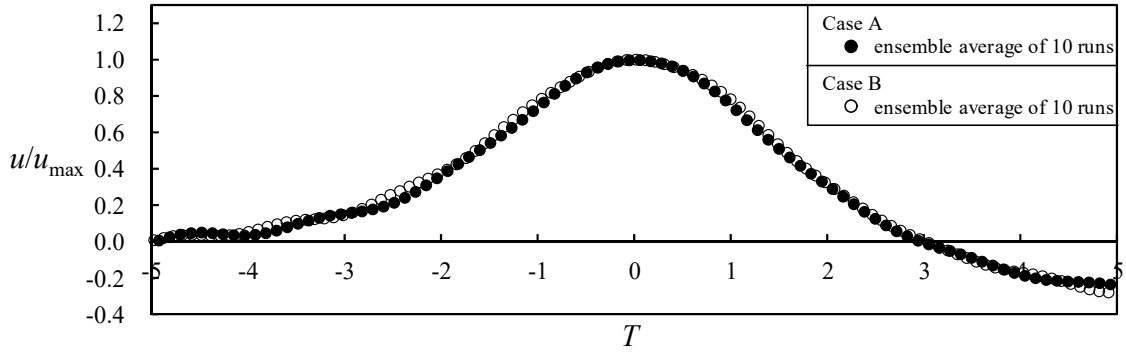

Figure 4. Comparison of the temporal variation of the non-dimensional horizontal velocity between Case A and Case B measured at (x/h_0, y/h_0) = (0, 0.94).

4.4. Breaker Type of Solitary Wave over Sloping Beach

The breaker type of a solitary wave traveling over a sloping beach can be identified using the slope parameter (Grilli et al. [7]), which is defined as $S^* = 1.521 \times S_0 \times (H_0/h_0)^{-1/2}$ with S_0 being the slope of the sloping beach. It is well known that, if $S^* > 0.37$, no breaking take places; and different breaker types (like surging, plunging or spilling breaker) appear for $S^* < 0.37$, depending on the value of S^*. For the present Cases A and B, the value of the S^* are identically equal to 0.842, which are both corresponding to the non-breaking solitary wave over the 1:3 sloping beach. It is evidently found that the breaker types for both cases do show good agreement with those identified by the slope parameter S^*, strongly indicating no discernible scale effect on the breaker type of solitary wave.

It should be noted that the dimension of the wave flume is relatively small, and the scales of the wave height and water depth are not large. However, fairly detailed examinations of the free surface elevation, the wave celerity, the velocity time series and the breaker type all clearly testify no apparent scale effect and existence of the Froude number similarity for the present two cases.

5. Test for Calculating Accelerations and Pressure Gradient Using Measured Velocity Data

5.1. Expressions for Accelerations and Pressure Gradient

Based on the incompressible Navier-Stokes equation of motion (Daily and Harleman [28]), the force per unit mass in the X direction is written as:

$$\begin{aligned} \partial U/\partial t + U\partial U/\partial X + V\partial U/\partial Y &= A_l(X, Y, t) + A_{c1}(X, Y, t) + A_{c2}(X, Y, t) \\ &= A_t(X, Y, t) \\ &= -(1/\varrho)\partial P/\partial X - g\partial H_P/\partial X + (\mu/\varrho)[\partial(\partial U/\partial X)/\partial X + \partial(\partial U/\partial Y)/\partial Y], \end{aligned} \tag{2}$$

in which A_l (=$\partial U/\partial t$) is the local acceleration, A_{c1} (=$U\partial U/\partial X$) and A_{c2} (=$V\partial U/\partial Y$) are the first and second convective accelerations and A_t (=$A_l + A_{c1} + A_{c2}$) is the total acceleration in the positive X direction, along with ϱ being the density of water, g the gravity acceleration, μ the dynamic viscosity and H_P the potential associated with the gravitational force. Note that the gravity term in Equation (2), $-g\partial H_P/\partial X$, is equal to $-g\sin\theta = -g \times 1/10^{1/2} = -310.2$ cm/s^2 in the positive X direction (see Figure 1b). In addition, the contribution of the term, $(\mu/\varrho)[\partial(\partial U/\partial X)/\partial X + \partial(\partial U/\partial Y)/\partial Y]$, is tested to be very small (to be stated later) and thus can be neglected in this study.

Once the (ensemble-averaged) velocity fields measured by HSPIV are obtained directly from the (X, Y) coordinate system or indirectly via the (x, y) coordinate system and then transformed into the former one, all the accelerations $A_l(X, Y, t)$, $A_{c1}(X, Y, t)$, $A_{c2}(X, Y, t)$ and $A_t(X, Y, t)$ can be computed by mainly using central difference scheme. Then a "partially depth-averaged" operation (i.e., excluding the velocity data obtained in the boundary layer or within a vortex flow) is adopted to get the partially depth-averaged values of accelerations, that is, $A_{l,da}(X, t)$, $A_{c1,da}(X, t)$, $A_{c2,da}(X, t)$ and $A_{t,da}(X, t)$, together with the partially depth-averaged value of pressure gradient $[(1/\varrho)\partial P/\partial X]_{da}$ based on Equation (2). Similar to the method used by Jensen et al. [12], a symmetric five-point smoothing scheme is utilized to smooth temporally the partially depth-averaged values of acceleration. Eventually, the smoothed values of accelerations, $A_{l,s}(X, t)$, $A_{c1,s}(X, t)$, $A_{c2,s}(X, t)$, $A_{c,s}(X, t)$ and $A_{t,s}(X, t)$ can be obtained. Accordingly, the smoothed value of pressure gradient corresponding to these accelerations in the onshore direction is expressed as follow:

$$\begin{aligned} [(1/\varrho)\partial P(X, t)/\partial X]_s &= -A_{l,s}(X, t) - A_{c1,s}(X, t) - A_{c2,s}(X, t) - g\partial H_P/\partial X \\ &= -[A_{t,s}(X, t) + g\partial H_P/\partial X] \\ &= P^*(X, t) \text{ (cm/s}^2\text{)}. \end{aligned} \tag{3}$$

From experimental point of view, obtaining accelerations is, however, more difficult than velocities due to very fast temporal and spatial fluctuations even in the fine PIV/HSPIV measurements (Jensen et al. [12,19]). Therefore, the influences of different time and spatial intervals on the values of accelerations should be tested and evaluated in the following subsections.

5.2. Calculation Example for Local Acceleration

The sampling frequency of the HSPIV measurements used in this subsection is 2000 Hz for the FOV$_1$, resulting in the time elapse between any two consecutive images being $\Delta t_{framing} = 0.0005$ s. The tests are performed by trial-and-error, using different time intervals, Δt, to compute the values of local acceleration, $A_l(X, Y, t)$ (=$\partial U/\partial t \approx \Delta U/\Delta t$). Accordingly, the effect of different time intervals can be assessed.

For easy comprehension, a calculation example is proposed with the values of the heights Y and the data for three (ensemble-averaged) velocity profiles $U(Y)$ obtained at $X = 18.81$ cm for $t = 0.6455$, 0.6545 and 0.6635 s being tabulated in order from the left side of Table A1 in Appendix A. Note that these velocity profiles, $U(Y)$ and $V(Y)$, obtained at the three time instants are also shown later in

Figure 8c. It is found that, at t = 0.6545 s with Δt = 0.0090 s (see the sixth column of Table A1), the computed values of $A_l(Y)$ at different heights Y do vary remarkably from −194.5 cm/s^2 to −76.6 cm/s^2, exhibiting their highly fluctuating feature in the Y direction. Herein, the partially depth-averaged method is used to calculate the representative value for the external stream at the specified section. Accordingly, the partially depth-averaged value of the local acceleration, $A_{l,da}$, is computed to be −116.8 cm/s^2 at t = 0.6545 s with Δt = 0.0090 s (listed at the bottom of the sixth column in Table A1).

Similarly, five additional different time intervals with Δt = 0.0045, 0.0135, 0.0180, 0.0225 and 0.0315 s (see the fifth and from the seventh to the tenth columns of Table A1) are tested with reference to t = 0.6545 s, however, all the corresponding velocity profiles are not shown here. The calculated values of $A_l(Y)$ even at the same heights for all of these five distinct time intervals are found to change drastically, revealing their highly fluctuating characteristic due to different time intervals used (Jensen et al. [12]). Moreover, the partially depth-averaged values of local acceleration, $A_{l,da}$, are correspondingly equal to −88.4, −111.9, −119.9, −117.1 and −132.9 cm/s^2 (all listed at the bottom of Table A1 and shown in Figure 5a). Herein, the promising range of Δt for obtaining the reasonable values of $A_{l,da}$ is identified as the one within which the relative deviation (D_r) of each result of $A_{l,da}$ would only vary within 4.0% with respect to a specified average. Note that the specified average is computed from the sum of each of $A_{l,da}$ only within the 4.0% criterion and then divided by the total qualified number. For example, the computed values of $A_{l,da}$ for Δt = 0.0090, 0.0135, 0.0180 and 0.0225 s (from the sixth to the ninth columns of Table A1) are equal to −116.8, −111.9, −119.9 and −117.1 cm/s^2 with an average of −116.4 cm/s^2. The relative deviations with respect to the average, D_r, for the four time intervals only vary from 0.34% up to 3.9% (see Table A1), as seen within the two dotted vertical lines in Figure 5a). Note that the two values of $A_{l,da}$ = −88.4 and −132.9 cm/s^2 for the smallest and largest time intervals employed (i.e., Δt = 0.0045 and 0.0315 s, see the fifth and tenth columns in Table A1) just reflect prominent biases from the average with the relative deviations D_r equal to 23.9% and 14.5% (see also Figure 5a) and are not considered as the reasonable estimates. These evidences do demonstrate that the reasonable values of $A_{l,da}$ can be obtained due to use of the appropriate time intervals with Δt = (0.0090–0.0225) s = (18–45) × $\Delta t_{framing}$ at t = 0.6545 s in the tests.

5.3. Calculation Example for First Convective Acceleration

The tests for computing the first convective acceleration, $A_{cl}(X, Y, t)$ (=$U\partial U/\partial X \approx U \times \Delta U/\Delta X$), are conducted also by trial-and-error, using distinct spatial intervals ΔX. Accordingly, the effects of different spatial intervals on the values of these accelerations can be evaluated. As seen from Table A2 in Appendix A, the values of the height Y and the data of the three (ensemble-averaged) velocity distributions $U(Y)$ measured at X = 17.85, 18.81 and 19.77 cm (i.e., with ΔX = 0.96 cm with respect to X = 18.81 cm) for t = 0.6545 s are listed in the four leftmost columns, respectively. The calculated results for the values $A_{cl}(Y)$ and $A_{cl,da}$ are listed in the ninth column with respect to ΔX = 0.96 cm. Further, four more spatial intervals with ΔX = 0.42, 0.60, 0.78 and 1.02 cm are tested. As observed in Table A2 (see from the sixth to the tenth columns), the computed values of $A_{c1,da}$ vary from 24.1 cm/s^2 to 26.1 cm/s^2 (with an average of 25.1 cm/s^2). The relative deviations with respect to the average, D_r, vary from 0.4% to 4.0% (see Table A2 and Figure 5b), exhibiting the promising range of ΔX to calculate the reasonable values of $A_{c1,da}$. However, for a smaller spatial interval (ΔX = 0.24 cm), the value of $A_{c1,da}$ are estimated to be 21.8 cm/s^2 (see the fifth column of Table A2); and for a larger spatial interval (ΔX = 1.38 cm), the counterpart is 29.8 cm/s^2 (see the eleventh column of Table A2). The relative deviations D_r are correspondingly equal to 13.1% and 18.7% (also see Table A2 and Figure 5b) with reference to the average (=25.1 cm/s^2), respectively, for t = 0.6545 s. The tests strongly testify that too smaller or larger spacing interval used does lead to considerable deviation from all the reasonable values of the first convective acceleration.

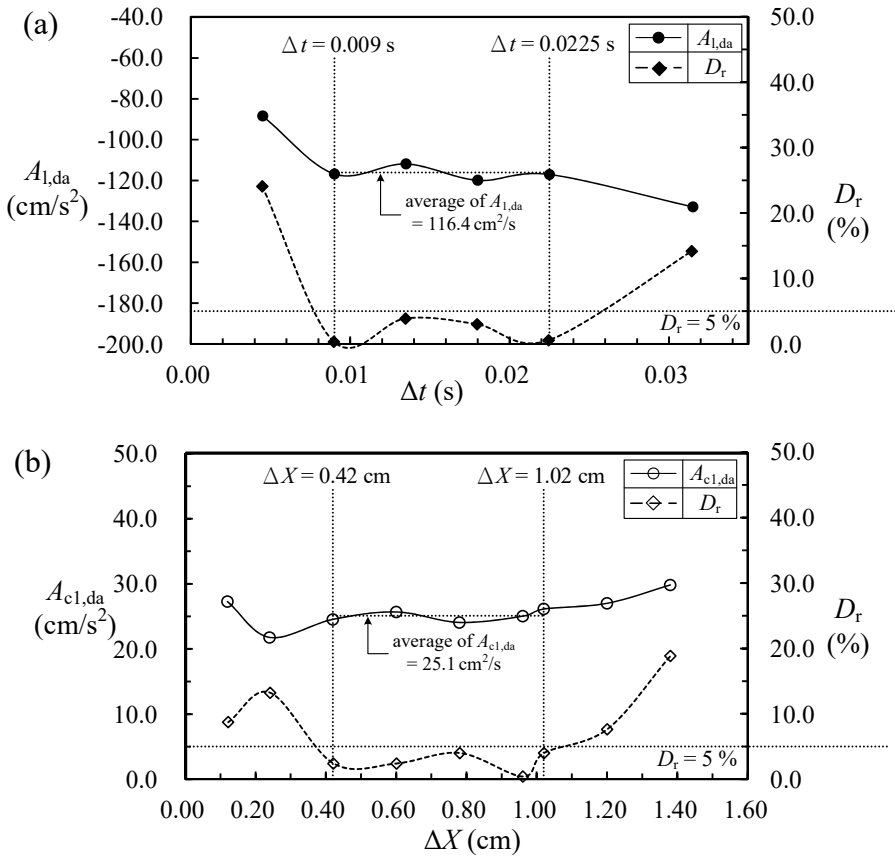

Figure 5. The calculation results and relative deviations for the partially depth-averaged values of (**a**) the local acceleration $A_{l,da}$ corresponding to different time intervals Δt used; and (**b**) the first convective acceleration $A_{cl,da}$ corresponding to distinct spatial intervals ΔX employed at t = 0.6545 s. The promising range of Δt or ΔX, within which the relative deviation D_r of each result of either $A_{l,da}$ or $A_{cl,da}$ would only vary within 4.0% with respect to the average, is marked between the two dotted vertical lines.

5.4. Calculation Example for Second and Total Accelerations as well as Pressure Gradient

For calculating the second convective acceleration, $A_{c2}(X, Y, t)$ (=$V\partial U/\partial Y \approx V \times \Delta U/\Delta Y$), only one spatial interval in the Y direction is used with ΔY = 0.060 cm for 0.6545 s ≤ t < 0.9390 s and ΔY = 0.022 cm for 0.9390 s ≤ t ≤ 1.1380 s, respectively. This is because of the use of two different FOVs with distinct pixel resolutions. Table A3 in Appendix A lists the values of the heights Y (here with ΔY = 0.06 cm), the (ensemble-averaged) velocity data ($U(Y)$, $V(Y)$), the corresponding values of the second convective acceleration $A_{c2}(Y)$, the total convection acceleration $A_c(Y)$, the total acceleration $A_t(Y)$ and the pressure gradient $(1/\varrho)\partial P(Y)/\partial X$ for X = 18.81 cm and t = 0.6545 s. In addition, the partially depth-averaged values of the accelerations with $A_{c2,da}$ = −1.2 cm/s², $A_{c,da}$ = 23.8 cm/s² and $A_{t,da}$ = −95.5 cm/s² as well as the partially depth-averaged values of pressure gradient with $[(1/\varrho)\partial P/\partial X]_{da}$ = −214.7 cm/s² are also furnished at the bottom of Table A3.

Based on the procedure mentioned above, different time intervals Δt and distinct spatial intervals ΔX are further tested for t = 0.7765, 0.8670, 1.0068 and 1.0385 s to obtain the reasonable values of $A_{l,da}$ and $A_{c1,da}$, which would not be subject to prominent changes due to small variation of the time and spatial intervals. Table 2 lists time t, the representative velocity U_r (i.e., the local maximum velocity near the free surface), the appropriate time interval used Δt, the calculated values of $A_{l,da}$ and $A_{c1,da}$ as well as their corresponding averages and relative deviations D_r and *the promising ranges* of Δt and ΔX for t = 0.6545–1.0385 s. The data sets given in Table 2 clearly show that the relative deviations, D_r, for the calculated values of $A_{l,da}$ and $A_{c1,da}$ are all less than 4.0%. Moreover, for t = 0.6547–1.0385 s, the value of $(\mu/\varrho)[\partial(\partial U/\partial X)/\partial X + \partial(\partial U/\partial Y)/\partial Y]$ is testified to be very small with (10^{-3}–10^{-4}) times the

gravity term (i.e., $-g\partial H_p/\partial X = -310.2$ cm/s^2) in Equation (2). Therefore, its contribution in Equation (2) can be neglected, thus resulting in Equation (3).

Table 2. A summary of the tested results for obtaining the reasonable values of $A_{l,da}$ and $A_{cl,da}$ with different Δt and ΔX, respectively, together with a list of the promising ranges of Δt and ΔX for t = 0.6545–1.0385 s (i.e., T = 7.25–11.50).

t (s)	T	U_r (cm/s)	Δt (s)	ΔT	$A_{l,da}$ (cm/s^2)	Average of $A_{l,da}$ (cm/s^2)	Relative Deviation D_r (%)	ΔX (cm)	$A_{cl,da}$ (cm/s^2)	Average of $A_{cl,da}$ (cm/s^2)	Relative Deviation D_r (%)	Suggested Range Δt (s)	Suggested Range ΔX (cm)
0.6545	7.25	−26.0	0.0090	0.10	−116.8	−116.4	0.3	0.42	24.5	25.1	2.4	0.0090–0.0225	0.42 – 1.02
			0.0135	0.15	−111.9		3.9	0.60	25.7		2.4		
			0.0180	0.20	−119.9		3.0	0.78	24.1		4.0		
			0.0225	0.25	−117.1		0.6	0.96	25.0		0.4		
								1.02	26.1		4.0		
0.7765	8.60	−37.2	0.0080	0.09	−101.3	−105.4	3.8	0.24	136.0	140.1	2.9	0.0080 – 0.0180	0.24 – 0.96
			0.0090	0.10	−108.0		2.5	0.42	144.4		3.1		
			0.0018	0.20	−106.8		1.4	0.60	140.3		0.2		
								0.96	139.5		0.4		
0.8670	9.60	−48.6	0.0070	0.08	−244.5	−243.9	0.3	0.12	543.2	540.6	0.5	0.0070 – 0.0180	0.12 – 0.42
			0.0080	0.09	−248.5		1.9	0.24	549.4		1.6		
			0.0090	0.10	−245.7		0.8	0.42	529.1		2.1		
			0.0180	0.20	−236.8		2.9						
1.0068	11.15	−100.0	0.0053	0.06	−968.7	−1004.3	3.5	0.11	2087.8	2068.0	1.0	0.0053 – 0.0180	0.11 – 0.31
			0.0090	0.10	−1001.6		0.3	0.20	2000.9		3.2		
			0.0133	0.15	−1024.7		2.0	0.31	2115.3		2.3		
			0.0180	0.20	−1022.1		1.8						
1.0385	11.50	−120.0	0.0090	0.10	−458.1	−446.2	2.7	0.20	1266.2	1284.2	1.4	0.0090 – 0.0180	0.20 – 0.40
			0.0133	0.15	−429.0		3.8	0.31	1298.6		1.1		
			0.0180	0.20	−451.4		1.2	0.40	1287.9		0.3		

It is worth mentioning that the time intervals tested herein cover the maximum ranges of Δt = 0.0070–0.0225 s = (14–45) × $\Delta t_{framing}$ = (14–45)/2000 s in the FOV$_1$ for 0.6550 s ≤ t < 0.9390 s and Δt = 0.0053–0.0180 s = (16–54) × $\Delta t_{framing}$ = (16–54)/3000 s in the FOV$_2$ and FOV$_3$ for 0.9390 s ≤ t < 1.1380 s. All of the tests are conducted for the solitary wave having the characteristic time and length scales (i.e., the wave period and length) of t_p = 1.21 s and $l_s = C_0 \times t_p$ = 125.1 cm for Case A, respectively. Herein, the wave period/length of a solitary wave is defined as the time/length cutoff with reference to a free surface elevation/displacement of 1.0% of the incident wave height (Liu et al. [30]; Sumer et al. [31]; Lin et al. [32]) even though the wave length/period is generally regarded as infinite in theory. In addition, Jensen et al. [19] studied the local accelerations of two periodic waves with the wave periods of t_p = 0.70 and 1.67 s by using $\Delta t = 5 \times \Delta t_{framing}$ = 0.06 s and $\Delta t = 8 \times \Delta t_{framing}$ = 0.064 s (i.e., with $\Delta t_{framing}$ = 0.012 and 0.008 s), respectively. A total of 11.7 and 26.1 values of local acceleration for both cases can be obtained during a wave cycle with the equivalent framing rates of 83.4 and 125.0 Hz). Namely, the present study and Jensen et al. [19] both used larger values of the time interval for minimizing the calculation errors from two neighboring velocity fields obtained from three consecutive HSPIV and PIV images.

6. Results and Discussion

6.1. End of Run-Up at t = 0.6545 s (T = 7.25) and Start of Run-Down at t = 0.6945 s (T = 7.69)

Figure 6a–d presents the spatio-temporal variation in the (ensemble-averaged) velocity fields of the solitary wave for 10.8 cm ≤ x ≤ 20.1 cm at t = 0.6145, 0.6545, 0.6945 and 0.7545 s (i.e., T = 6.80, 7.25, 7.69 and 8.355), respectively, for Case A. Note that t = 0.6545 s identifies the moment for the end of the run-up phase at which the swash front (Baldock et al. [33]; Nielsen [34]) of the solitary wave exactly reaches the maximum run-up height. As seen in Figure 6a,b, the velocities of the water particles are all negative and the flow is undergoing the run-down motion in the offshore direction at t = 0.6145 and 0.6545 s for 10.8 cm ≤ x ≤ 20.1 cm. However, during this time interval between t = 0.6145 and 0.6545 s, the tip of the swash front is found to keep heading onshore to its maximum extent. For easy understanding, the corresponding images of the motion of swash front with reference to Figure 6a–d are shown in Figure 7a–d, respectively, for 39.8 cm ≤ x ≤ 49.6 cm. It is thus realized that,

even the swash front still advances toward onshore (see Figure 7a,b), all of the horizontal velocity components shown in the velocity fields (see Figure 6a,b) have taken negative values. These observations also indicate the phase-lead of the offshore velocity field over the onshore propagation of swash front, thus evidencing the offshore/onshore stream as seen in Figures 6a,b and 7a,b. As reported in Lin et al. [15], such a feature is characterized by the flow demarcation curve, which extends from the free surface down to the beach surface. Right on the flow demarcation curve, all of the horizontal velocities are equal to zero but with the negative/positive velocities on the offshore/onshore side of this curve.

As further seen in Figure 6b,c, the velocity fields keep exhibiting the offshore motion for all the water particles over the sloping beach. It is surprisingly found from Figure 7b,c that the tip or contact point of swash front remains at a fixed position but with its local free surface profile changing from the bull-nose shape (Nielsen [34]) into a sharp-edged one during the very short time interval between t = 0.6545 s and t = 0.6945 s. This phenomenon is produced by the effect of the interaction among the surface tension of water, the gravity force and viscous drag on the free surface of swash front very close to the contact point (at which the three phases of water, air and the solid sloping beach intersects together). Note that such a flow feature has also been reported in the paragraph IV in p.326 of Park et al. [35] for a solitary wave reflected from a vertical wall. Moreover, as seen in Figures 6c,d and 7c,d, the velocity fields exhibit again the successive run-down flow with increasing offshore velocities and the wave characterized by the sharp-edged free surface undergoes the early stage of run-down motion for t > 0.6945 s.

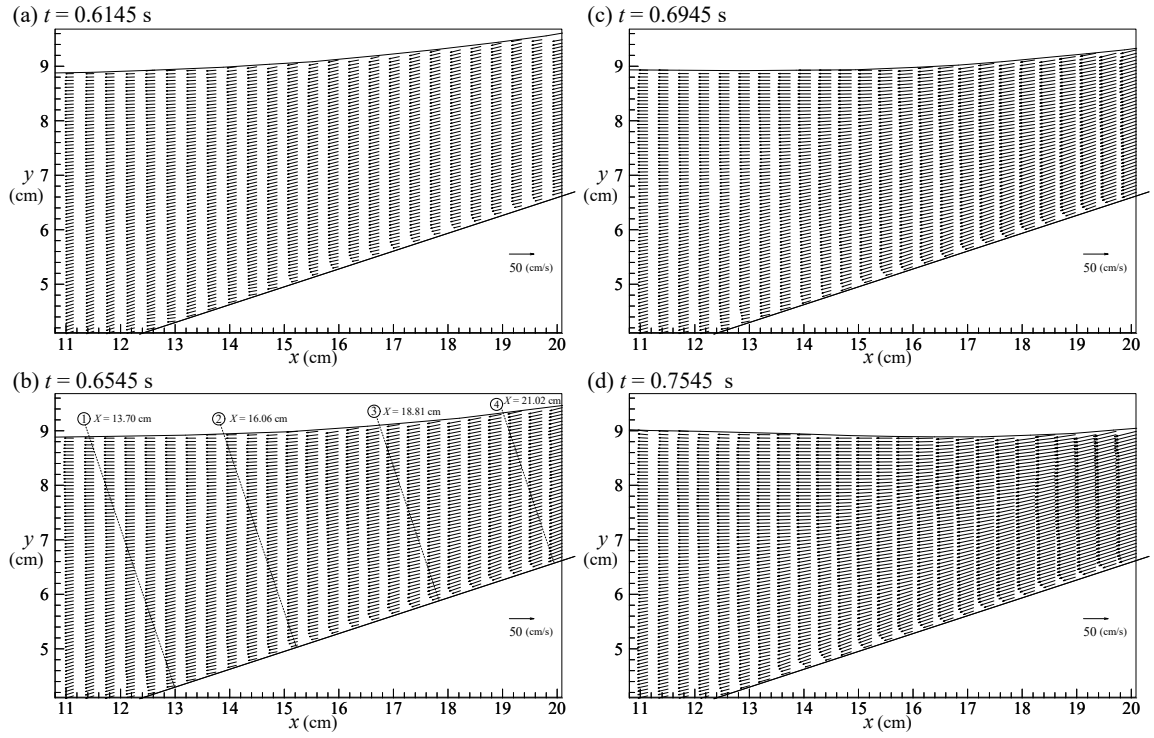

Figure 6. The spatio-temporal variation of the velocity field for t = (**a**) 0.6145 s; (**b**) 0.6545 s; (**c**) 0.6945 s; and (**d**) 0.7545 s. The velocity profiles $U(Y)$, obtained at four different positions X as shown in (**b**) each with an inclined line and a circled number, are shown later in Figure 8. Note that the incipient flow separation takes place on the beach surface for X = 18.81 cm (see the inclined line with ③ in (**b**)) at later time, t = 0.9210 s.

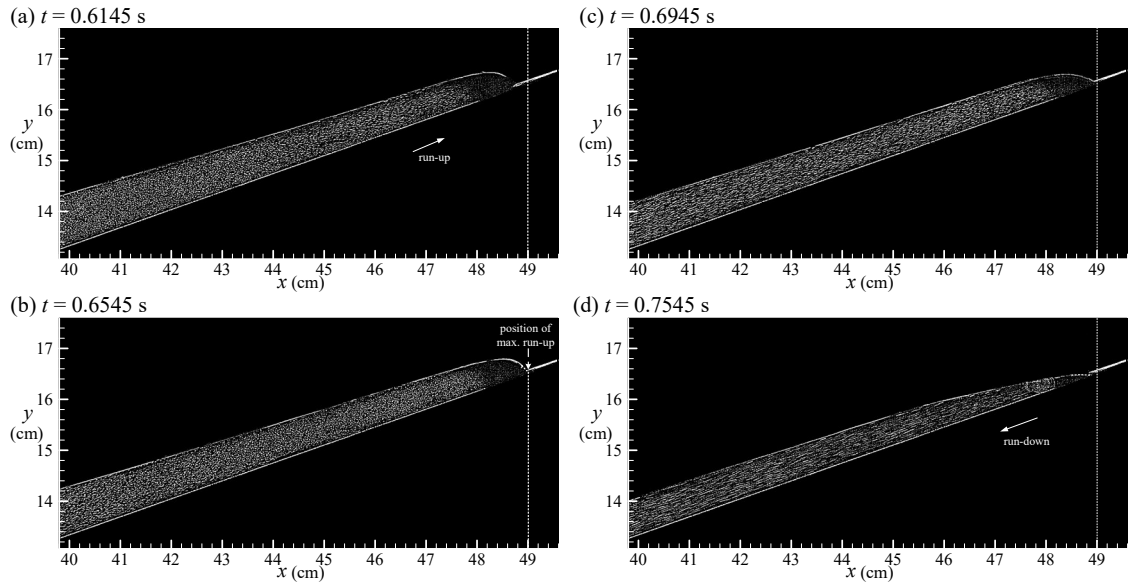

Figure 7. Four visualized images showing the propagation of solitary wave over the sloping beach at t = (**a**) 0.6145 s with run-up motion heading to the maximum run-up height; (**b**) 0.6545 s with the tip of swash front exactly reaching the maximum run-up height; (**c**) 0.6945 s with the tip of swash front staying at a nearly identical position as that at t = 0.6545 s, however, the water particles transporting offshore; and (**d**) 0.7545 s with the tip of free surface and water particles all moving offshore.

Following the approach adopted by Chow [25], Subramanya [26] and Henderson [36], the velocity component parallel with and the water depth normal to the sloping beach should be used to represent the corresponding characteristic for a flow moving over a sloping boundary. Accordingly, Figure 8a–d shows the profiles of $U(Y)$ for t = 0.6545 s, obtained at four distinct shoreward distances X as illustrated in Figure 6b with four inclined lines (normal to water surface) each having a circled number (from ① to ④). It is found that the distribution of $U(Y)$ is either quasi-linear or fairly uniform but excluding that close to the beach surface. Herein, the uniform or partially-depth-averaged velocity, $U_u(X, t)$ is defined as the mean of the velocities (parallel to the sloping beach) $U(Y)$ only within the quasi-linear or uniform part in the whole velocity profile. This part is, in fact, corresponding to the "external stream" of retreating flow, that is, without taking the velocities inside boundary layer flow (i.e., "internal stream" of the retreating flow) into account. Note that variation of $U_u(X, t)$ can be used as an indicator for acceleration or deceleration of the external stream of retreating flow.

As shown in Figure 8a–d, the magnitude of the (offshore) uniform velocity U_u decreases continuously from 27.1 cm/s, via 25.6 and 20.4 cm/s, to 18.8 cm/s with decreasing shoreward distance from X = 21.02 cm, via X = 18.81 and 16.06 cm, to X = 13.70 cm, respectively. These data indicate that the external stream of the retreating flow is decelerated spatially at t = 0.6545 s due to the convective acceleration (Daily and Harleman [28]) being negative in the offshore direction. More interestingly, as observed in Figure 8c for X = 18.81 cm, the magnitude of U_u increases with increasing t for t = 0.6455–0.6635 s. This observation strongly reveals that the external stream is accelerated temporally at t = 0.6545 s because the local acceleration (Daily and Harleman [28]) is positive in the offshore direction.

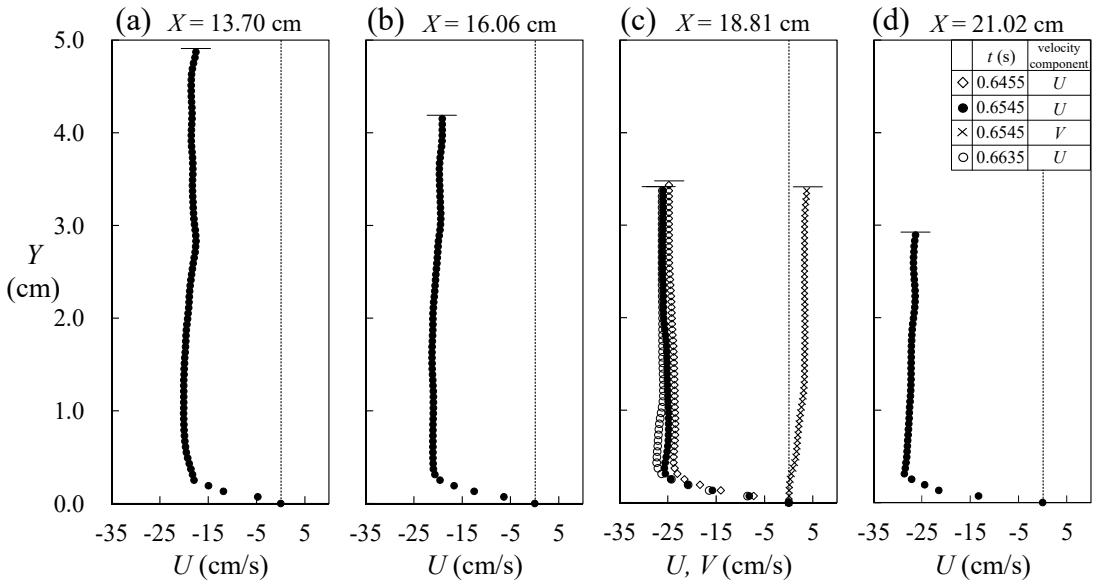

Figure 8. (**a**–**d**) The velocity profiles, $U(Y)$, obtained at four different shoreward distances, X, as marked in Figure 6b each with inclined line having a circled number (from ① to ④). Two additional velocity profiles $U(Y)$ for t = 0.6455 and 0.6635 s as well as one velocity profile $V(Y)$ for t = 0.6545 s are also included in (**c**). Note that selection of the four shoreward distances for these velocity profiles aims to highlight the variation trend of the uniform velocity on the onshore and offshore sides of X = 18.81 cm, at which the incipient flow separation occurs at later time t = 0.9210 s.

As seen from Table A1 in Appendix A, the four leftmost columns list the values of the heights Y, the data of the three ensemble-averaged velocity profiles $U(Y)$ at t = 0.6455, 0.6545 and 0.6635 s. In addition, the corresponding values of the local acceleration $A_l(Y)$, obtained with Δt = 0.0090 s using central difference scheme, are tabulated in the sixth column, show very drastic variation in the magnitudes at different heights. The depth-averaged value of the local acceleration is correspondingly presented with $A_{l,da}$ = −116.8 cm/s² at the bottom of the sixth column. Similarly, the values of $A_{l,da}(t)$ at different times can be obtained for X = 18.81 cm. For example, $A_{l,da}$ = −152.2, −146.2, −66.7 and −98.7 cm/s² at t = 0.6365, 0.6455, 0.6635 and 0.6725 s, respectively. A symmetric five-point smoothing scheme with different weightings (i.e., 1/6 for the front two, 1/3 for the targeted one and 1/6 for the rear two) is then employed in time domain. Accordingly, the smoothed value of the local acceleration at t = 0.6545 s is calculated to be $A_{l,s}$ = −116.3 cm/s².

In addition, the four leftmost columns of Table A2 in Appendix A show the values of the heights Y, the data of the three velocity profiles $U(Y)$ at X = 17.85, 18.81 and 19.77 cm for t = 0.6545 s. Further, the corresponding values of the first convective acceleration $A_{cl}(Y)$ acquired with ΔX = 0.96 cm using central difference scheme are listed in the eighth column. Accordingly, the partially depth-averaged values of the first convective acceleration is shown at the bottom of the eighth column with $A_{cl,da}$ = 25.0 cm/s² for X = 18.81 cm at t = 0.6545 s. Similarly, the values of $A_{cl,da}(t)$ at distinct times can be also acquired. For example, at t = 0.6365, 0.6455, 0.6635 and 0.6725 s, $A_{cl,da}$ = 30.8, 38.1, 16.1 and 34.7 cm/s², respectively. Similarly, the identical five-point smoothing scheme is again employed. The smoothed value of the first convective acceleration for X = 18.81 cm at t = 0.6545 s is therefore calculated to be $A_{cl,s}$ = 28.3 cm/s².

Furthermore, Table A3 in Appendix A lists the values of Y, the data of $V(Y)$ and $U(Y)$, the values of the second convective acceleration $A_{c2}(Y)$ with ΔY = 0.06 cm, the total convection acceleration $A_c(Y)$ [=$A_{c1}(Y) + A_{c2}(Y)$], the total acceleration A_t [=$A_l(Y) + A_c(Y)$] and the pressure gradient $(1/\varrho)\partial P(Y)/\partial X$ all obtained at different Y for X = 18.81 cm and t = 0.6545 s. The partially depth-averaged values of these accelerations with $A_{c2,da}$ = −1.2 cm/s², $A_{c,da}$ = 23.8 cm/s² and $A_{t,da}$ = −95.5 cm/s² as well as the counterpart of pressure gradient with $[(1/\varrho)\partial P/\partial X]_{da}$ = −214.7 cm/s² are all furnished at the bottom of Table A3 for X = 18.81 cm and t = 0.6545 s. Similarly, the values of $A_{c2,da}(t)$, $A_{c,da}(t)$ and $A_{t,da}(t)$ at different times can be obtained for X = 18.81 cm (not shown). Again, using the identical five-point smoothing scheme,

the smoothed values of the second convective acceleration, the total convective acceleration and the total acceleration are estimated to be $A_{c2,s}$ = −1.2 cm/s², $A_{c,s}$ = 27.1 cm/s² and $A_{t,s}$ = −89.2 cm/s², respectively. From Equation (3), the smoothed counterpart of the pressure gradient at X = 18.81 cm is computed to be P^* = $[(1/\varrho)\partial P/\partial X]_s$ = −221.0 cm/s² in the onshore direction. It is thus confirmed again that the external stream of the retreating flow is decelerated spatially under an adverse pressure gradient of $-P^*$ = 221.0 cm/s² in the offshore direction at t = 0.6545 s.

6.2. Early and First-Half Middle Stages of Run-Down for 0.6945 s < t ≤ 0.9210 s (7.69 < T ≤ 10.20)

As shown in Figure 7c, the early stage of run-down motion occurs for t > 0.6945 s, leading to the retreating flow triggered by gravity force. The overall retreating flow, including the shallowest free surface part, hereafter undergoes an evolution of run-down motion along the sloping beach. The velocity fields for 10.8 cm ≤ x ≤ 20.1 cm are shown in Figure 9a–d at t = 0.7405, 0.8125, 0.8850 and 0.9210 s (i.e., T = 8.20, 9.00, 9.80 and 10.20), respectively. As observed from these four velocity fields, the magnitude of the (offshore) uniform velocity, U_u, decreases spatially in the offshore direction at a specified T and the counterpart increases in the shallower zone with increasing T. It is thus confirmed that the external stream of retreating flow is decelerated spatially/accelerated temporally in the offshore direction during the time interval between t = 0.7405 s and t = 0.9210 s.

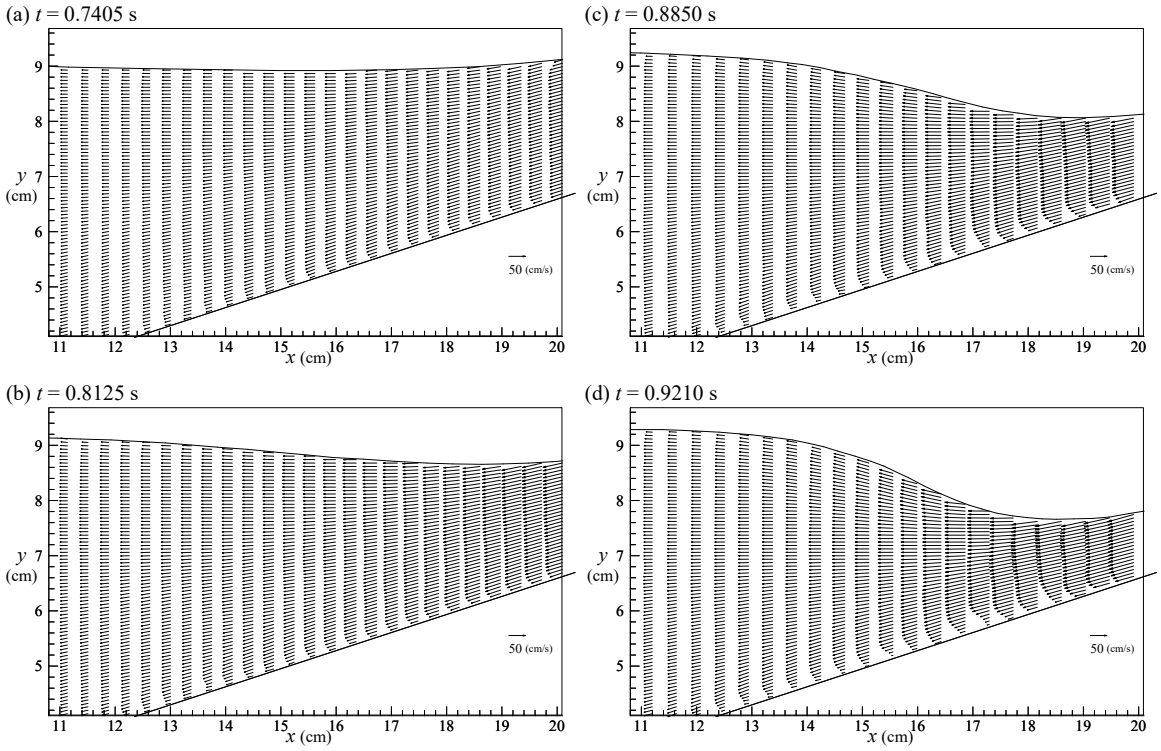

Figure 9. The spatio-temporal variation of the free surface profiles and the velocity fields at t = (**a**) 0.7405 s; (**b**) 0.8125 s; (**c**) 0.8850 s; and (**d**) 0.9210 s.

Similar to the computations adopted for t = 0.6545 s as serially shown in Tables A1–A3, the smoothed value of the local acceleration in the onshore direction at t = 0.8125 s (T = 9.00) is calculated to be $A_{l,s}$ = −128.9 cm/s² based on the velocity data obtained for t = 0.8035, 0.8125 and 0.8215 s at X = 18.81 cm (not shown). In addition, the smoothed values of the first and second convective accelerations are estimated to be $A_{c1,s}$ = 219.5 cm/s² and $A_{c2,s}$ = 11.8 cm/s², respectively, from the velocity fields (with ΔX = 0.60 cm and ΔY = 0.06 cm) at t = 0.8125 s and X = 18.81 cm. Accordingly, the smoothed value of the pressure gradient can be computed to be P^* = $[(1/\varrho)\partial P/\partial X]_s$ = −412.6 cm/s² in the onshore direction. This again demonstrates that the external stream of retreating flow is decelerated in space under an adverse pressure gradient of $-P^*$ = 412.6 cm/s² > 0 in the offshore direction. Note that the magnitude of this adverse pressure gradient (=412.6 cm/s²) at t = 0.8125 s is much larger than that (=221.0 cm/s²) at t = 0.6545 s. This strongly reveals that prominent flow deceleration takes place

spatially beneath the streamlined free surface profile (see Figure 9b,c) with increasing adverse pressure gradient.

Using the velocity profiles $U(Y)$ for t = 0.9120, 0.9210 and 0.9300 s (i.e., T = 10.10, 10.20 and 10.30) and $V(Y)$ for t = 0.9210 s at X = 18.81 cm (Figure 10b) as well as additionally acquired at X = 18.39 and 19.23 cm for t = 0.9210 s (Figure 10a,c), the smoothed values of the local acceleration and the two convective accelerations for t = 0.9210 s can be estimated to be $A_{l,s}$ = −370.3 cm/s², $A_{c1,s}$ = 726.7 cm/s² and $A_{c2,s}$ = 40.9 cm/s², respectively. Therefore, the pressure gradient P^* can be computed to be −707.5 cm/s² in the onshore direction. These data obviously highlight the retreating flow decelerated spatially and accelerated temporally in the offshore direction under an adverse pressure gradient of $-P^*$ = 707.5 cm/s² at $X = X_{ifs}$ = 18.81 cm. Note that the non-dimensional adverse pressure gradient $-P^*/g$ at the position of the incipient flow separation is equal to −0.721 for t = 0.9210 s. In summary, the adverse pressure gradient, $-P^*$ = 707.5 cm/s² is far larger than those for t = 0.6545–0.8850 s (i.e., 221.0–657.0 cm/s²), eventually resulting in occurrence of the incipient flow separation for t = 0.9210 s at $X = X_{ifs}$ = 18.81 cm. As reported by Lin et al. [1], the incipient flow separation occurs at t = 0.9210 s (T = 10.20) for $X = X_{ifs}$ = 18.81 cm, at which $\partial U/\partial Y$ has been first examined to be zero near the beach surface (Schlichting [37]).

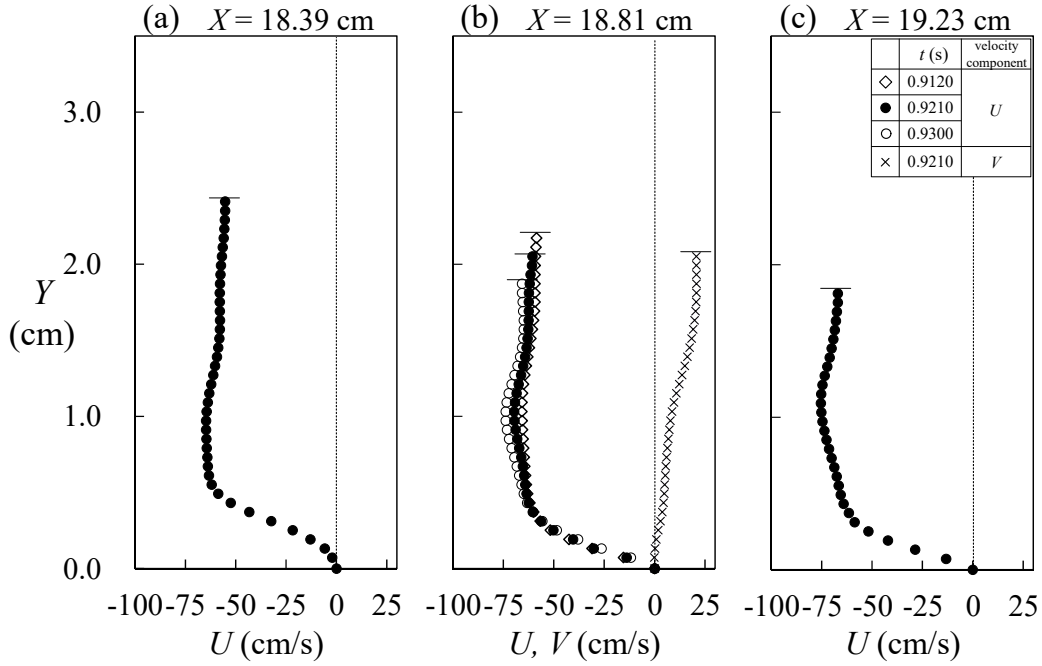

Figure 10. (**a**–**c**) The velocity profiles, $U(Y)$, measured at X = 18.39, 18.81 and 19.23 cm for t = 0.9210 s, respectively. Note that two velocity profiles, $U(Y)$, for t = 0.9120 and 0.9300 s as well as one velocity profile, $V(Y)$, at t = 0.9210 s are also included in (**b**).

6.3. Second-Half Middle Stage of Run-Down for 0.9210 s < t ≤ 1.0630 s (10.20 < T ≤ 11.77)

Soon after the incipient flow separation for t > 0.9210 s, the adverse pressure gradient causes the fluid particles to move away from the beach surface and transport toward the external stream of retreating flow. Then, it displaces in a direction opposite to the external stream, thus resulting in a very thin recirculation zone under the separated shear layer. Figure 11a,b/c,d presents two streaklined/pathlined images associated with development of the primary vortex under the separated shear layer for t = 0.9710 and 1.0010 s (i.e., T = 10.75 and 11.085), respectively. Figure 12a,b illustrates two instantaneous near-bottom velocity fields with nearly identical times being remarked in Figure 11a,b/c,d, respectively. As seen in Figure 11a,b/c,d and 12a,b, not only the curling streakline but also the pathlined recirculation zone with the onshore velocities very close to the beach surface can be identified near X = 17.0–19.0 cm. The curling streakline shown in Figure 11a,b reflects the growth of separated shear layer beneath which the fluid particles adjacent to the beach surface move in a

direction opposite to the external stream. Further, Figure 12a,b does reveal that the (offshore) uniform velocity $U_u(Y)$ decreases spatially and increases temporally in the offshore direction. This highlights the formation of primary vortex under the separated shear layer and confirms again the spatial deceleration of the retreating flow.

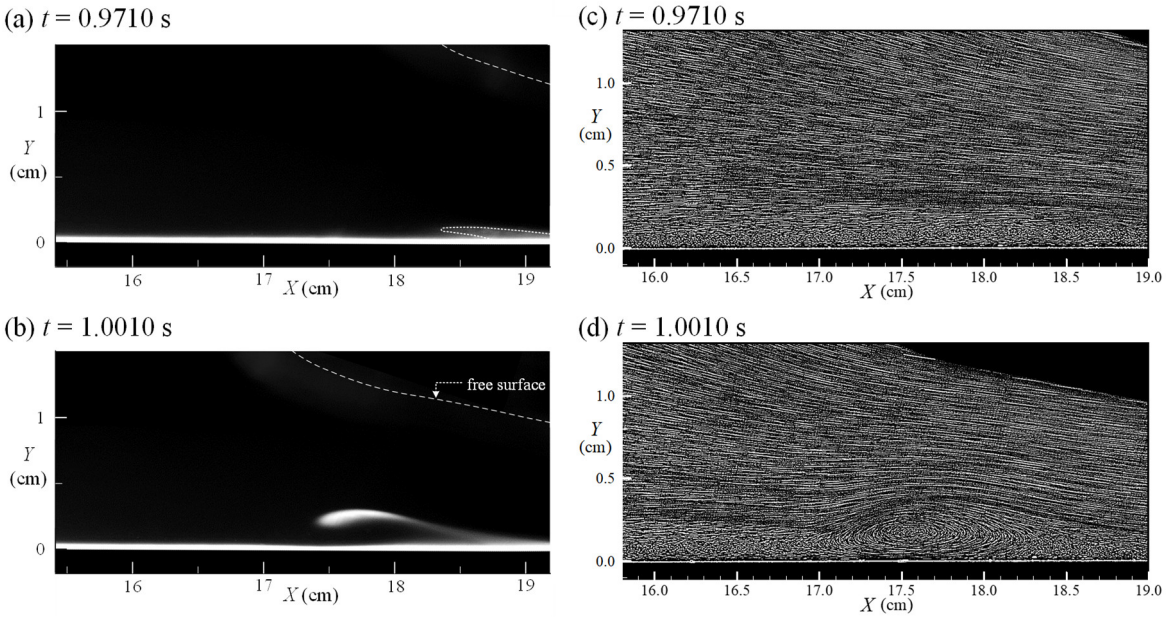

Figure 11. The streaklined and pathlined images (displayed in the left and right panels, respectively) showing growth of the separated shear layer and development of the primary vortex at t = (**a**,**c**) 0.9710 s; and (**b**,**d**) 1.0010 s.

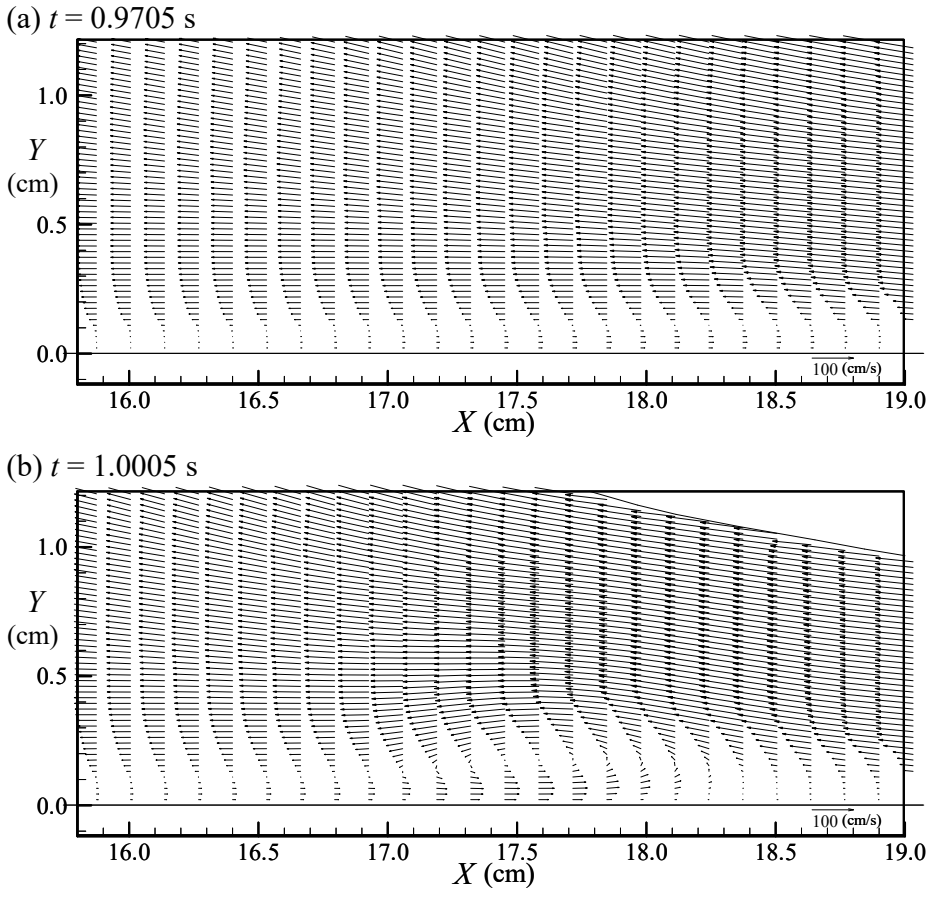

Figure 12. The instantaneous near-bottom velocity fields at t = (**a**) 0.9705 s; and (**b**) 1.0005 s.

Figure 13a presents three free surface profiles obtained at t = 0.9978, 1.0068 and 1.0158 s (i.e., T = 11.05, 11.15 and 11.25) for 10.8 cm ≤ x ≤ 20.2 cm, over which abrupt rise in the free surface is seen around x = 14.4–15.6 cm at t = 1.0068 s (T = 11.15). This feature, in fact, marks the onset of hydraulic jump (Chow [25]; Subramanya [26]; Sumer et al. [27]). As clearly beveled in Figure 13a, the corresponding close-ups of the ensemble-averaged velocity fields are shown in Figure 13b–d. The well-organized primary vortex structure evolves with its core centering at the "core section" (where the primary vortex core is positioned instantaneously), that is, $X = X_{co}$ = 17.62, 17.41 and 17.20 cm for t = 0.9978, 1.0068 and 1.0158 s, respectively. Figure 14a shows the vorticity contour, $\Gamma(X, Y)$ (=$\partial V(X, Y)/\partial X - \partial U(X, Y)/\partial Y$), for the primary vortex and two accompanied eddies appearing on its both sides for 0 cm < Y < 0.83 cm at t = 1.0068 s. Note that the peak vorticity having a value of $\Gamma = \Gamma_{pv}$ = 477.0 s^{-1} occurs at $(X, Y) = (X_{pv}, Y_{pv})$ = (17.36, 0.31) cm, which is located above the primary vortex core (X_{co}, Y_{co}) = (17.41, 0.20) cm (see Figure 14b). Namely, the height that corresponds to the peak vorticity, Y_{pv} = 0.31 cm, is situated beyond the "core height" at $Y = Y_{co}$ = 0.20 cm but below the "size height" at $Y = Y_{size}$ = 0.36 cm. The size height is, herein, identified as the height gauged from the beach surface, via the core of primary vortex and along the positive Y direction, then up to a typical point at which the outermost streamline enclosing the primary vortex is nearly merging with but still parallel to the characteristic streamline arising from the separation point or saddle point (Lin et al. [1]). Figure 14b illustrates the distributions of both the vorticity, Γ and the shear stress divided by dynamic viscosity, $\tau(X, Y)/\mu$ (=$\partial V(X, Y)/\partial X + \partial U(X, Y)/\partial Y$), at X_{co} = 17.41 cm for t = 1.0068 s. It can be thus confirmed that the maximum value of Γ and the negative maximum of τ/μ both occur at the same height of Y_{pv} = 0.31 cm, which is larger than Y_{co} = 0.20 cm and smaller than Y_{size} = 0.36 cm.

Figure 15a–c, presents three profiles of $U(Y)$ obtained at X = 17.21, 17.41 and 17.61 cm for t = 1.0068 s, respectively. Further, two additional velocity profiles $U(Y)$ for t = 0.9978 and 1.0158 s and one additional counterpart $V(Y)$ for t = 1.0068 s all obtained at X = 17.41 cm are shown in Figure 15b. It is found that the maximum velocity and the (offshore) uniform velocity both increase spatially with decreasing water depth or increasing shoreward distance X.

Accordingly, the smoothed value of local acceleration for the external stream of retreating flow at t = 1.0068 s (T = 11.15) can be calculated to be $A_{l,s}$ = −977.1 cm/s² in the onshore direction. This implies relatively large value of positive acceleration in the offshore direction and thus drastic increase in the offshore velocity $U(Y)$ at the core section, X_{co} = 17.41 cm. The two convective accelerations are estimated to be $A_{c1,s}$ = 1895.3 cm/s² and $A_{c2,s}$ = 71.5 cm/s² in the onshore direction. Accordingly, the smoothed value of the pressure gradient in the external stream for t = 1.0068 s can be obtained with P^* = −1299.9 cm²/s being the favorable pressure gradient in the onshore direction, that is, $-P^*$ = 1299.9 cm²/s being the adverse pressure gradient in the offshore direction at the core section. This indicates that very prominent deceleration of the external stream still occurs up to t = 1.0068 s under the adverse pressure gradient equal to $-P^*/g$ = 1.325. It is pertinent to note that, as compared with this adverse pressure gradient (=1299.9 cm/s²) right at X_{co} = 17.41 cm for t = 1.0068 s, two larger values of the counterparts having $-P^*$ = 2287.0 cm/s² and 2748.5 cm/s² are surprisingly found to appear at X = 17.08 cm and 17.76 cm, respectively. The reason can be guided to more prominent flow decelerations in the offshore direction, which are actually resulted from the external stream being highly decelerated spatially under very large magnitudes of the first convective accelerations and moderately accelerated temporally under fairly large values of the local accelerations.

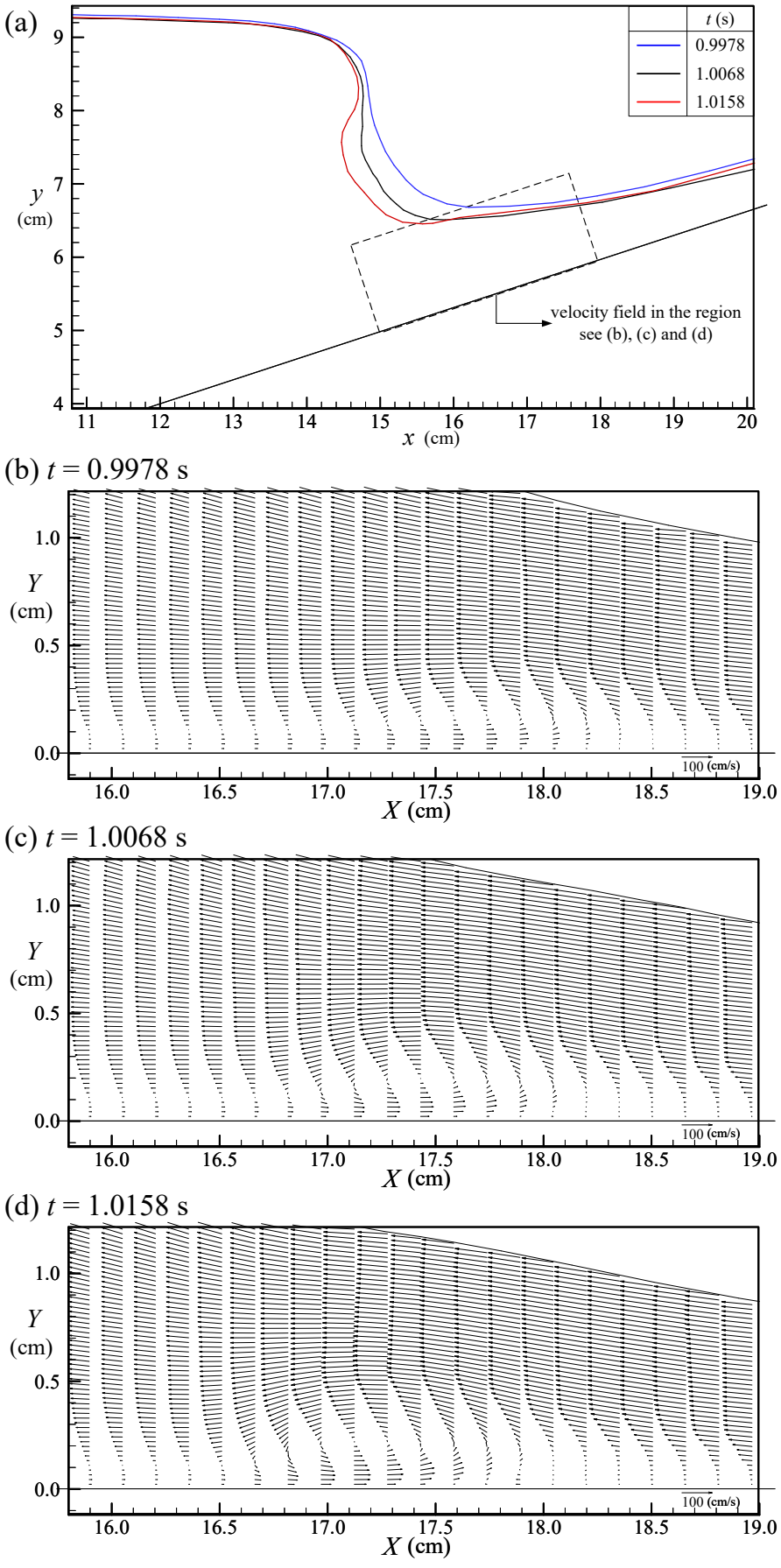

Figure 13. (**a**) The free surface profiles obtained at t = 0.9978, 1.0068 and 1.0158 s. The near-bottom velocity fields at t = (**b**) 0.9978 s; (**c**) 1.0068 s; and (**d**) 1.0158 s.

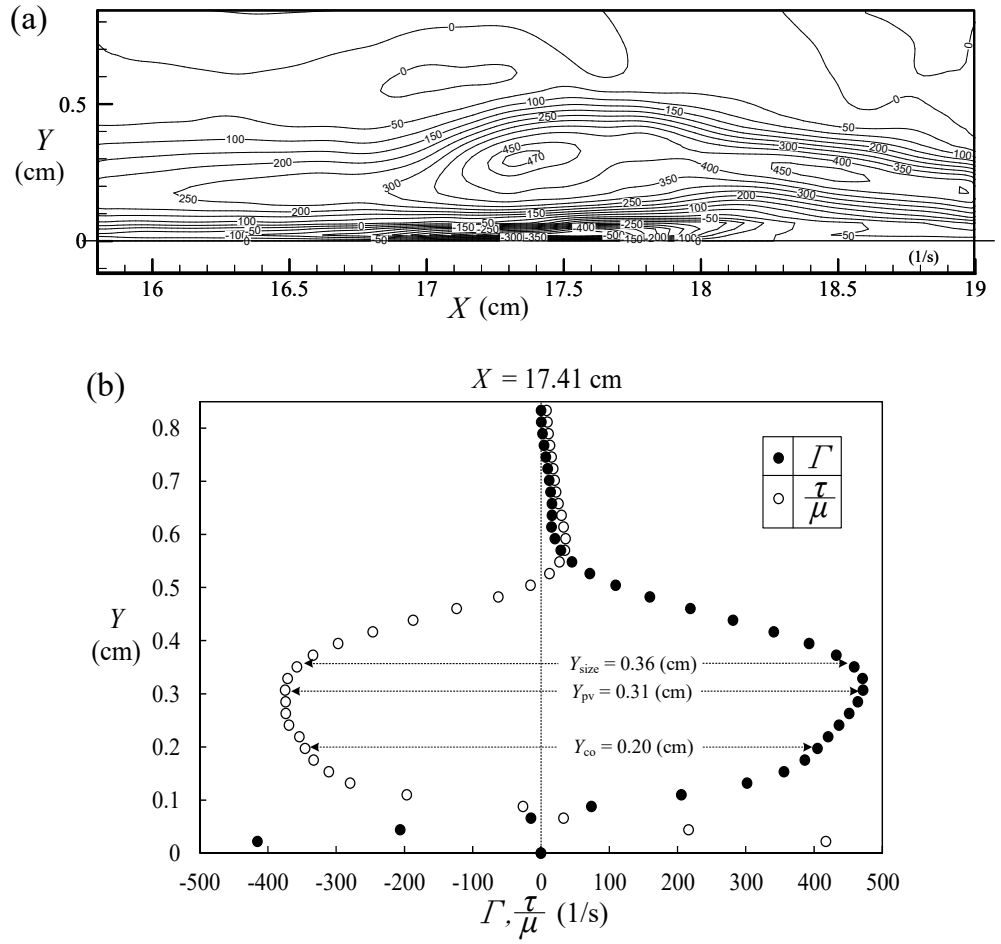

Figure 14. (**a**) Distribution of the vorticity contour, $\Gamma(X, Y)$, around the primary vortex (unit in 1/s); (**b**) distributions of both the vorticity, $\Gamma(Y)$ and the shear stress divided by the dynamic viscosity, $\tau(Y)/\mu$, at X_{co} = 17.41 cm for t = 1.0068 s.

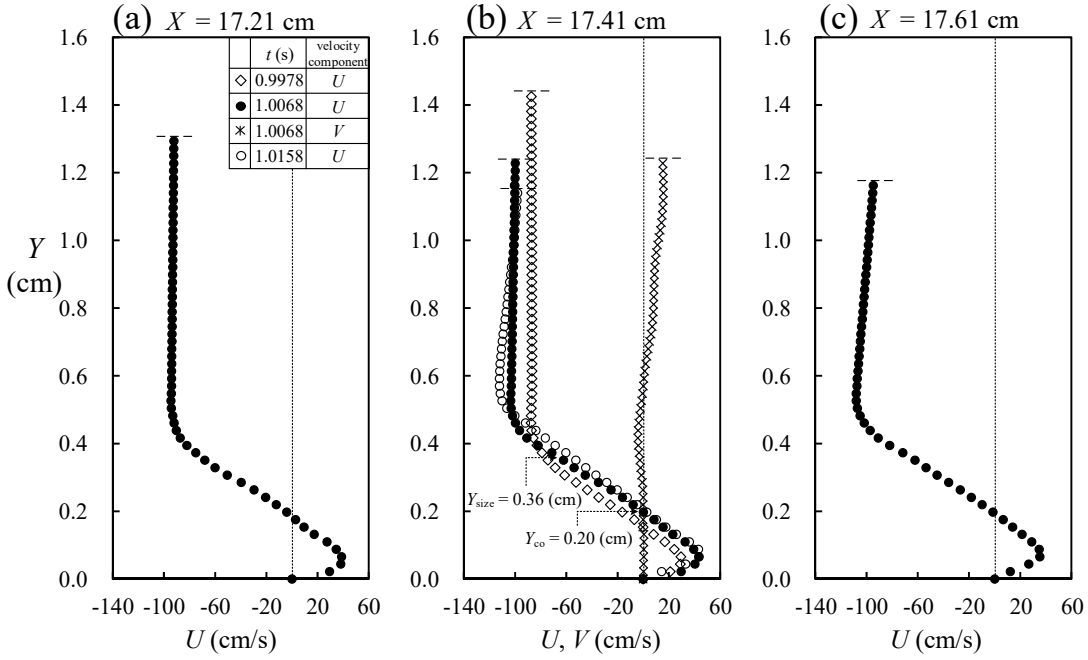

Figure 15. (**a**–**c**) The velocity profiles $U(Y)$ measured at X = 17.21, 17.41 and 17.61 cm for t = 1.0068 s, respectively. Note that two velocity profiles, $U(Y)$, for t = 0.9978 and 1.0158 s as well as one velocity profile, $V(Y)$, at t = 1.0068 s are also included in (**b**).

Figure 16 presents the spatio-temporal variation of the free surface profiles obtained at t = 1.0205, 1.0340, 1.0475 and 1.0610 s (i.e., T = 11.30, 11.45, 11.60 and 11.75), respectively, for 10.8 cm ≤ x ≤ 20.2 cm. Figure 17a–d/e–h shows four streakline/pathline patterns of the evolving primary vortex under the separated shear layer, which are corresponding to the free surface profiles with the identical times shown in Figure 16. As observed in Figure 16, during this time interval, the projecting jet stemming from the curling motion on the tip of the free surface is developing. Meanwhile, due to persistent acceleration of the external stream in the supercritical retreating flow (Lin et al. [1]), the primary vortex subsequently evolves with increasing size height. It should be mentioned that elaborated examination of the two-dimensionality of flow field has been demonstrated in Lin et al. [1]. They have also confirmed that evolution of the primary vortex, which presents a smoothly silk-like streakline pattern, does highlight the vortex flow nearly without exhibiting turbulence (i.e., being laminar). As seen in Figure 17a–d/e–h, the size heights of primary vortex are estimated to be Y_{size} = 0.42, 0.49, 0.57 and 0.62 cm, respectively. In addition, formation of the secondary and finer vortices beneath the separated shear layer for 16.8 cm ≤ X ≤ 17.8 cm is also noticed.

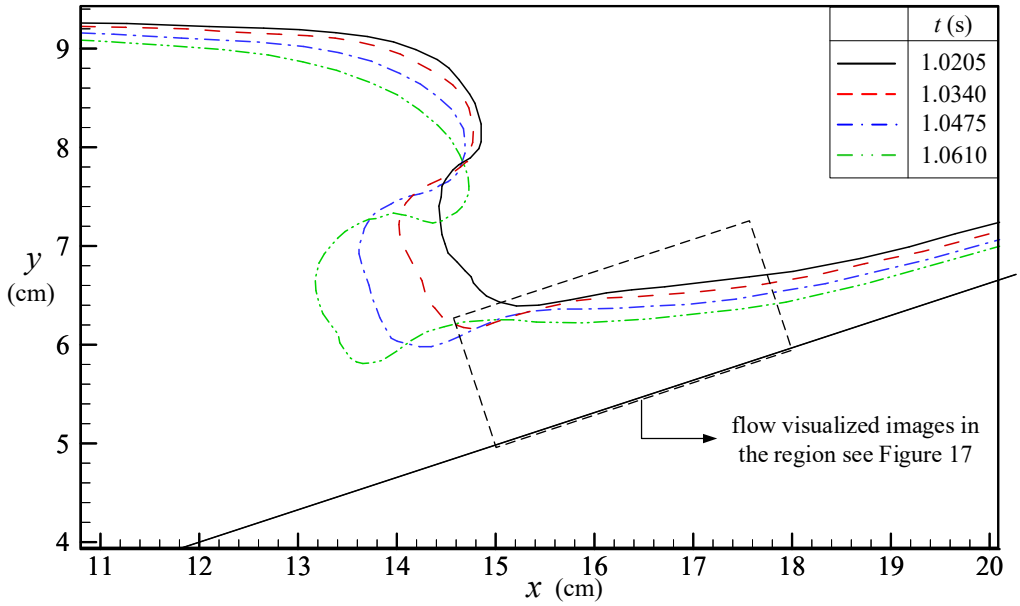

Figure 16. The free surface profiles obtained at t = 1.0205, 1.0340, 1.0475 and 1.0610 s.

6.4. Late Stage of Run-Down Motion for 1.0629 < t ≤ 1.2130 s (11.77 < T ≤ 13.43)

Figure 18a present the free surface profiles obtained at t = 1.0718, 1.0775 and 1.0832 s (i.e., T = 11.87, 11.93 and 11.995) for 10.8 cm ≤ x ≤ 20.1 cm. Figure 18b–d shows the corresponding velocity fields for 13.3 cm ≤ X ≤ 16.5 cm (marked in Figure 18a). As seen in Figure 18a–d and indicated in Lin et al. [1], the high-speed external stream, which has higher offshore speed than the "convection velocity (i.e., the mean velocity of the vortex core moving offshore within a time elapse)" of the primary vortex, first impinges upon the primary vortex due to the relative obstruction of the primary vortex, next jumps rapidly over the onshore and top side of the primary vortex with distinguishable curvature and then slides down the offshore side of the primary vortex. Namely, the high-speed external stream acts like a free-jump flow surrounding and over the primary vortex, then like a free-flop flow moving down the offshore side of the primary vortex.

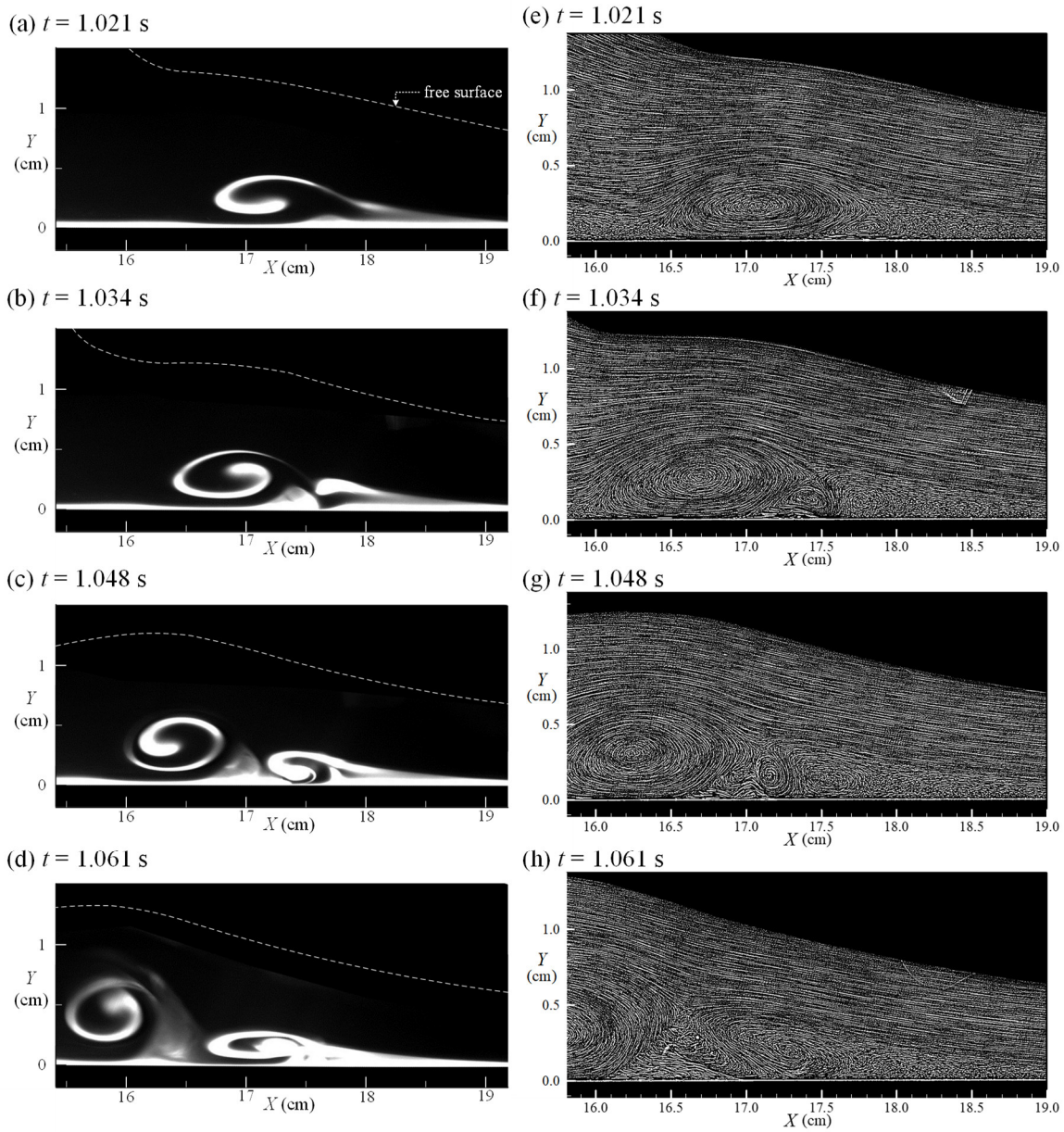

Figure 17. The streaklined and pathlined images (displayed in the left and right panels, respectively) showing evolution of the primary vortex at t = (**a**,**e**) 1.021 s; (**b**,**f**) 1.034 s; (**c**,**g**) 1.048 s; and (**d**,**h**) 1.061 s.

Based on the three velocity profiles obtained at $X = X_{co} = 14.98$ cm for $t = 1.0718$, 1.0775 and 1.0832 s ($T = 11.87$, 11.93 and 11.995) as seen in Figure 19b, the smoothed value of local acceleration for the external stream at $t = 1.0775$ s is calculated to be $A_{l,s} = 2076.5$ cm/s^2. This result highlights prominently temporal increase/decrease in the onshore/offshore velocity $U(Y)$ of the external stream, accompanied by considerable rise of the free surface in the vicinity of the core section, $X_{co} = 14.98$ cm (i.e., $x_{co} = 14.21$ cm) (see Figure 18a). Moreover, by using two velocity profiles $U(Y)$ obtained at $X = 14.78$ and 15.18 cm as well as one velocity profile $V(Y)$ given at $X_{co} = 14.98$ cm (Figure 19a–c) for $t = 1.0775$ s, the smoothed values of convective accelerations are computed to be $A_{c1,s} = -580.6$ cm/s^2 and $A_{c2,s} = 166.3$ cm/s^2. Under such a situation, P^* is calculated to be −1972.4 cm/s^2 (i.e., a favorable pressure gradient) in the onshore direction or alternatively $-P^* = 1972.4$ cm/s^2 (i.e., an adverse pressure gradient) in the offshore direction for $t = 1.0775$ s.

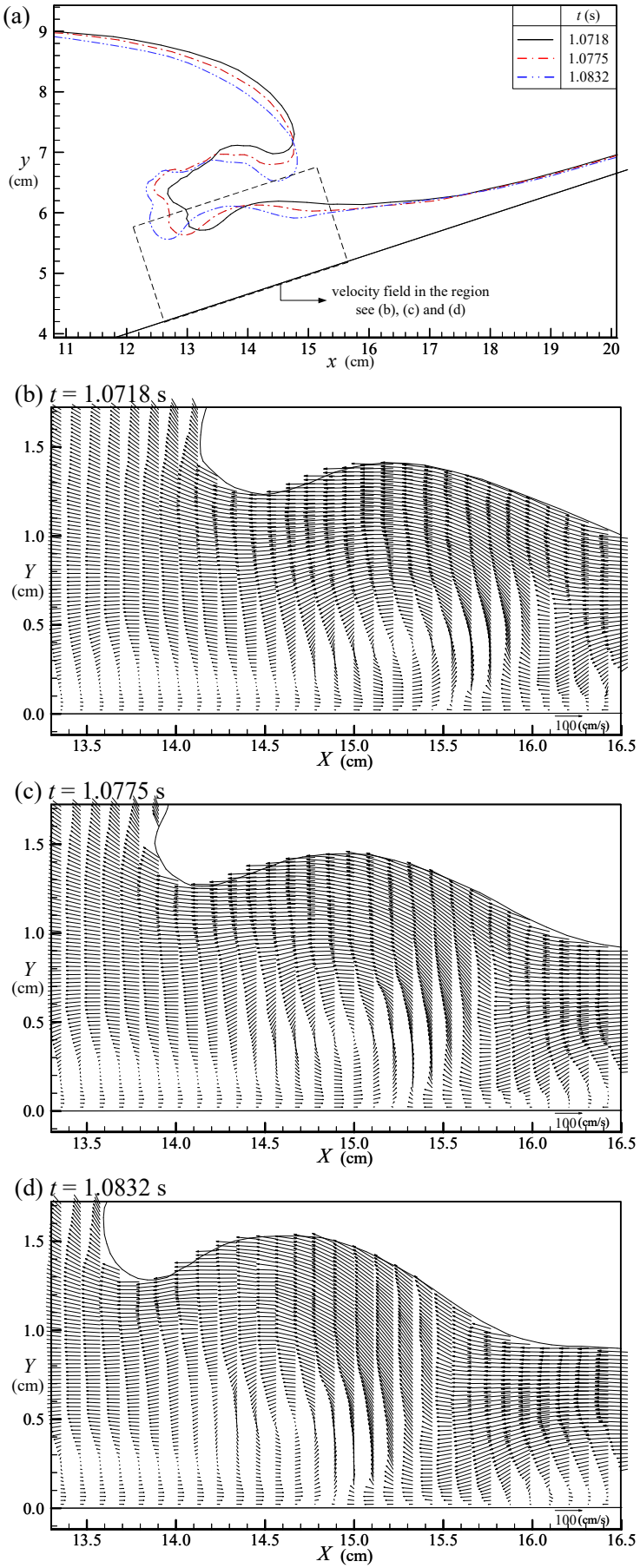

Figure 18. (**a**) The free surface profiles obtained at t = 1.0718, 1.0775 and 1.0832 s. The velocity fields in the vicinity of the primary vortex at t = (**b**) 1.0718 s; (**c**) 1.0775 s; and (**d**) 1.0832 s.

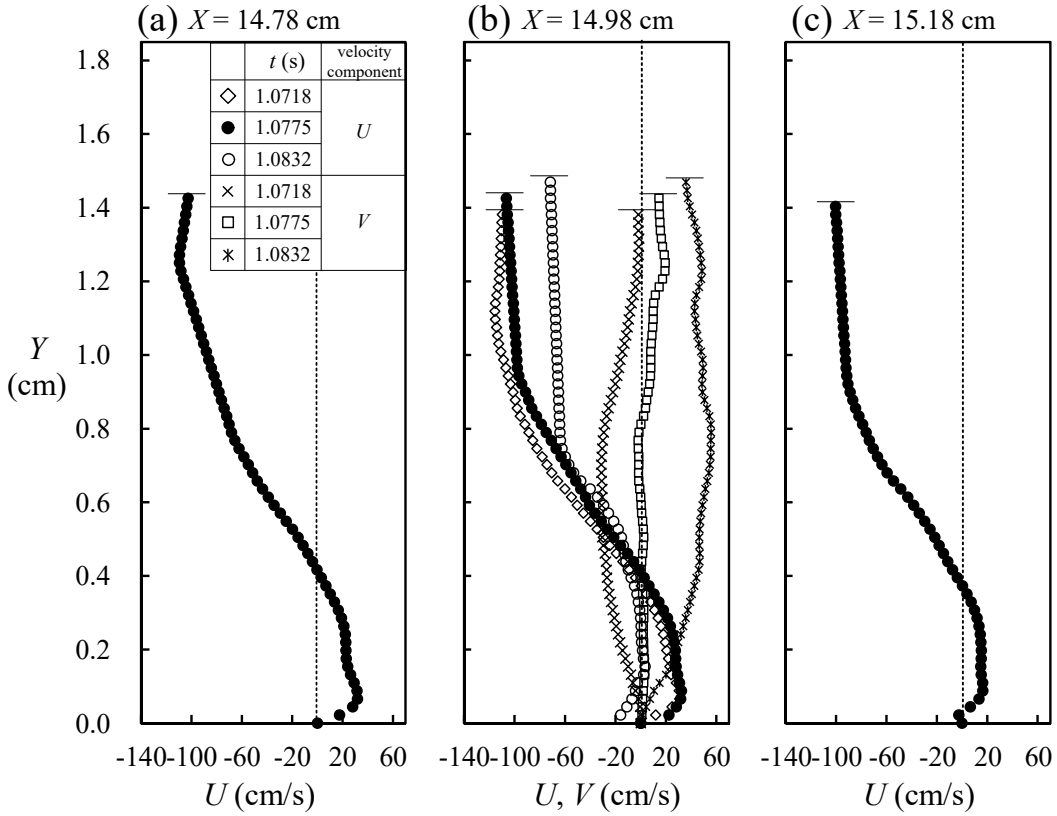

Figure 19. (**a**–**c**) The velocity profiles $U(Y)$ measured at X = 14.78, 14.98 and 15.18 cm for t = 1.0775 s, respectively. Note that two velocity profiles, $U(Y)$, for t = 1.0718 and 1.0832 s as well as three velocity profiles, $V(Y)$, at t = 1.0718, 1.0775 and 1.0832 s are also included in (**b**).

Herein, the evidence of $-P^*/g$ = 2.011 at t = 1.0775 s indicates extremely prominent adverse pressure gradient (which is larger than two times of gravity acceleration) and the flow severely decelerated in the offshore direction. Under such a situation, prominent rise of the free surface (see Figure 18a) and sudden increase of the vertical velocity around t = 1.0775 s should occur at this core section (see Figure 19b). As a further supporting evidence, the partially depth-averaged value of local acceleration in the vertical direction $A_{lv,da}$ (=$(\partial V/\partial t)_{da}$) for the external stream is calculated by using three vertical velocity profiles $V(Y)$ for t = 1.0718, 1.0775 and 1.0832 s at X_{co} = 14.98 cm (see Figure 19b). It is surprisingly found that the local acceleration in the vertical direction is equal to $A_{lv,da}$ = 3305.7 cm/s^2 > 0 (i.e., $A_{lv,da}/g$ = 3.37). The result strongly reconfirms the evident rise of the free surface at X_{co} = 14.98 cm for t = 1.0775 s and reveals very rapid change from negative, via nearly zero, to positive vertical velocity for 1.0718 s ≤ t ≤ 1.0832 s.

6.5. Summary of Variations in Non-Dimensional Convection Velocity, Vorticity, Accelerations and Pressure Gradient

As indicated by Lin et al. [1], the non-dimensional shoreward distance of the core section, X_{co}/h_0, decreases as T (=$t \times (g/h_0)^{1/2}$) increases for 10.55 ≤ T ≤ 12.11, namely, the primary vortex moves further offshore with increasing T (see Figure 18 in that article). It is interesting to note that the differentiation of X_{co}/h_0 with respect to T, that is, $d(X_{co}/h_0)/dT = (dX_{co}/dt)/(gh_0)^{1/2} = U_{cv}/C^*$ denotes the ratio of the convection velocity U_{cv} to the linear wave celerity C^* (=$(gh_0)^{1/2}$). As shown in Figure 20, the magnitude of the non-dimensional convection velocity, U_{cv}/C^*, increases linearly from 0.06 at T = 10.55, via 0.55 at T = 11.93, to 0.63 at T = 12.16.

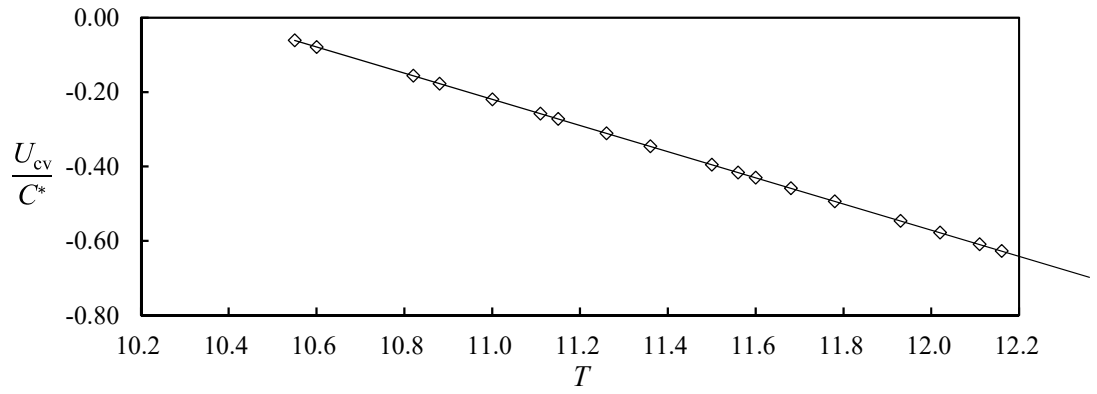

Figure 20. Variation of the non-dimensional convection velocity of the primary vortex core, U_{cv}/C^*, with the non-dimensional time, T.

Figure 21 illustrates temporal variation of the non-dimensional accelerations and pressure gradient, $A_{l,s}/g$, $A_{c,s}/g$, $A_{t,s}/g$ and P^*/g for $7.25 \le T \le 10.20$ at $X = X_{ifs} = 18.81$ cm before occurrence of the incipient flow separation. It is found that all the non-dimensional local accelerations, $A_{l,s}/g$, have negative values in the onshore direction (namely, $-A_{l,s}/g$, being positive in the offshore direction) and their magnitudes increase from 0.119 at $T = 7.25$ to 0.377 at $T = 10.20$, highlighting the retreated flow is more accelerated temporally in the offshore direction. In addition, the non-dimensional convective accelerations $A_{c,s}/g$, as also shown in Figure 21, all take positive/negative values and increase in magnitude with increasing T in the onshore/offshore direction. For example, the increase in $A_{c,s}/g$ from 0.028 at $T = 7.25$ to 0.782 at $T = 10.20$ exhibits the retreated flow more accelerated/decelerated spatially in the onshore/offshore direction. Moreover, due to the local/convective acceleration being negative/positive with different magnitudes, respectively, the values of the non-dimensional total acceleration $A_{t,s}/g$ are negative for $7.25 \le T < 8.30$ but positive for $8.30 \le T \le 10.20$ in the onshore direction. Note that $A_{t,s}/g$ is equal to −0.091 at $T = 7.25$, 0 at $T = 8.29$ and 0.405 at $T = 10.20$, respectively.

According to Equation (3), the magnitude of the non-dimensional favorable pressure gradient $P^*/g < 0$ in the "onshore" direction increases with increasing T for $7.25 \le T < 10.20$. Namely, the values of non-dimensional adverse pressure gradient $-P^*/g > 0$ in the "offshore" direction are 0.225 at $T = 7.25$ and 0.721 at $T = 10.20$. This fact further confirms that the retreating flow is subject to increasing adverse pressure gradient and more decelerated spatially with increasing T in the offshore direction, thus leading to occurrence of the incipient flow separation at $X = X_{ifs} = 18.81$ cm for $t = 0.9210$ s ($T = 10.20$).

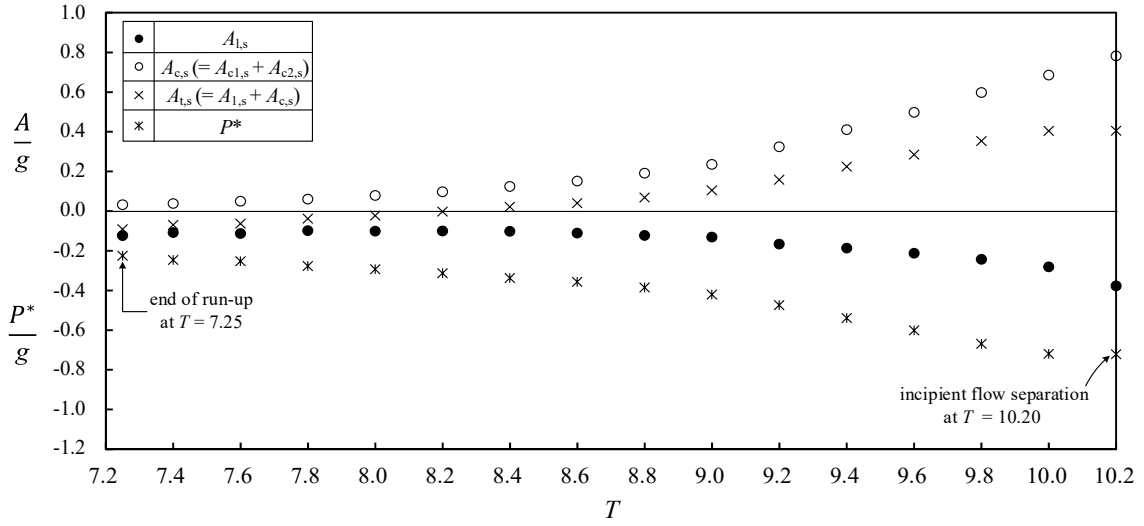

Figure 21. Variations of the smoothed values of the local acceleration $A_{l,s}$, the convective acceleration $A_{c,s}$, the total acceleration $A_{t,s}$ and the pressure gradient P^* in the onshore direction at X = 18.81 cm versus the non-dimensional time, T, for $7.25 \le T \le 10.20$.

Figure 22 presents the variations in $A_{l,s}/g$, $A_{c,s}/g$ and $A_{t,s}/g$ for the external stream of retreating flow calculated at each core section for $10.20 \le T \le 12.56$. It is found that $A_{l,s}/g$ decreases from −0.377 at T = 10.20 to a negative maximum of −0.996 at T = 11.15 (i.e., the instant at which hydraulic jump occurs), then increases successively to zero at about T = 11.63. For $11.63 < T \le 12.56$, $A_{l,s}/g$ increases from zero to a positive maximum of 2.117 at T = 11.93 and then decreases continuously down to zero and −0.581 at T = 12.31 and 12.56, respectively. Note that $A_{l,s}/g \approx -1.0$ for $11.00 < T < 11.20$ and $A_{l,s}/g > 1.0$ for $11.76 < T < 12.16$, clearly demonstrating the magnitude of the local acceleration larger than the gravity acceleration.

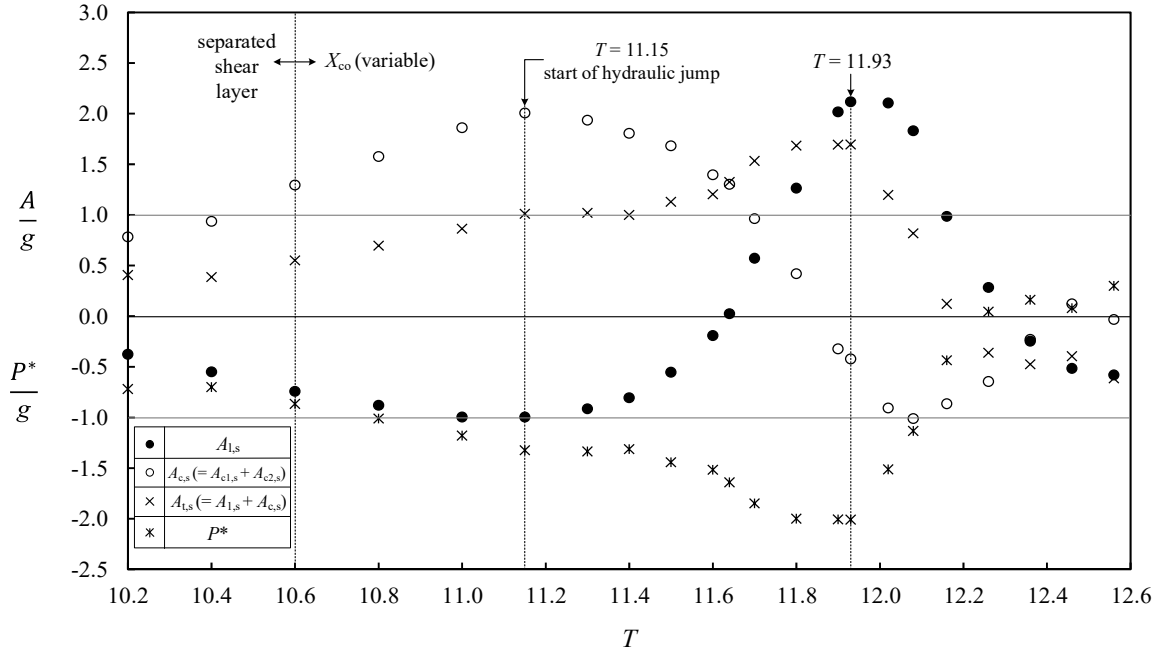

Figure 22. Variations of the smoothed values of the local acceleration $A_{l,s}$, the convective acceleration $A_{c,s}$, the total acceleration $A_{t,s}$ and the pressure gradient P^* in the onshore direction at the core section versus the non-dimensional time, T, for $10.20 \le T < 12.60$.

As also seen in Figure 22, the non-dimensional convective acceleration $A_{c,s}/g$ increases consecutively from 0.782 at T = 10.20 to a positive maximum of 2.005 at T = 11.15 (i.e., the instant for occurrence of hydraulic jump), then decreases successively down to 0 at T = 11.86. Afterwards, $A_{c,s}/g$ takes negative value with increasing magnitude down to a negative maximum of −1.013 at T = 12.08 and then with decreasing magnitude up to −0.034 at T = 12.56. It can be thus summarized that, for $10.20 \le T \le 11.63$, the negative/positive maximum of local/convective acceleration (i.e., $-0.996g/2.005g$) occurs at T = 11.15. On the other hand, for $11.63 \le T \le 12.56$, the positive/negative maximum of local/convective acceleration (i.e., $2.117g/-1.013g$) takes place at T = 11.93/12.08.

Further, it is also evidenced in Figure 22 that the non-dimensional total acceleration $A_{t,s}/g$ of the external stream increases consecutively from 0.405 at T = 10.20, via 1.009 at T = 11.15, to a positive maximum of 1.694 at T = 11.93; and then decreases continuously, via zero at about T = 12.29, to −0.615 at T = 12.56. Finally, the non-dimensional pressure gradient P^*/g of the external stream (in the onshore direction) is obviously seen from Figure 22 to decrease successively from −0.721 at T = 10.20, via −1.325 at T = 11.15, to a negative maximum of −2.011 at T = 11.93 and then to increase consecutively, via zero at about T = 12.25, to 0.299 at T = 12.56. Note that $-P^*/g$ = 2.011 at T = 11.93 demonstrates clearly decelerated flow in the offshore direction under the considerable adverse pressure gradient, thus

resulting in evident rise of the free surface and sudden increase of the vertical velocity, as shown in Figures 18a and 19b.

Figure 23 illustrates the relationship between the temporal variation in the non-dimensional peak vorticity of the separated shear layer $\Gamma_{pv}/[g/h_0]^{1/2}$ or the vorticity of the primary vortex core $\Gamma_{co}/[g/h_0]^{1/2}$ and the temporal variation in the non-dimensional, smoothed value of the local acceleration $A_{l,s}/g$. As evidenced from visualized images shown for T = 10.20, the peak vorticity corresponding to the incipient flow separation, Γ_{pv}, should be equal to zero. It is seen clearly that $\Gamma_{pv}/[g/h_0]^{1/2}$ increases quasi-linearly with increasing T for 10.20 < T < 10.60 and then $\Gamma_{co}/[g/h_0]^{1/2}$ that forms increases with increase in T for about 10.60 ≤ T ≤ 11.63. The maximum value of the non-dimensional vorticity, $[\Gamma_{co}/(g/h_0)^{1/2}]_{max}$ = 42.2, appears at T = 11.63 approximately. Then $\Gamma_{co}/[g/h_0]^{1/2}$ keeps decreasing with further increase of T for 11.63 < T ≤ 12.56. The main reason for having such a feature can be attributable to the acceleration ($-A_{l,s} > 0$) and deceleration ($-A_{l,s} < 0$) of the high-speed external stream in the offshore direction within the interval of 10.20 ≤ T ≤ 11.63 and 11.63 < T ≤ 12.56, respectively (see Figure 23). Because the strength of primary vortex (in terms of vorticity at vortex core) is enhanced by the entrainment of energy supply from the accelerated high-speed external stream, via the separated shear layer, into the vortex structure during the acceleration phase. However, the primary vortex strength is reduced by the detrainment of energy from the vortex structure, via the separated shear layer, into the decelerated external stream during the deceleration phase. Note that such a variation trend is analogous to the situation in the recirculation zone behind an impulsively-started circular cylinder (Lin et al. [38]).

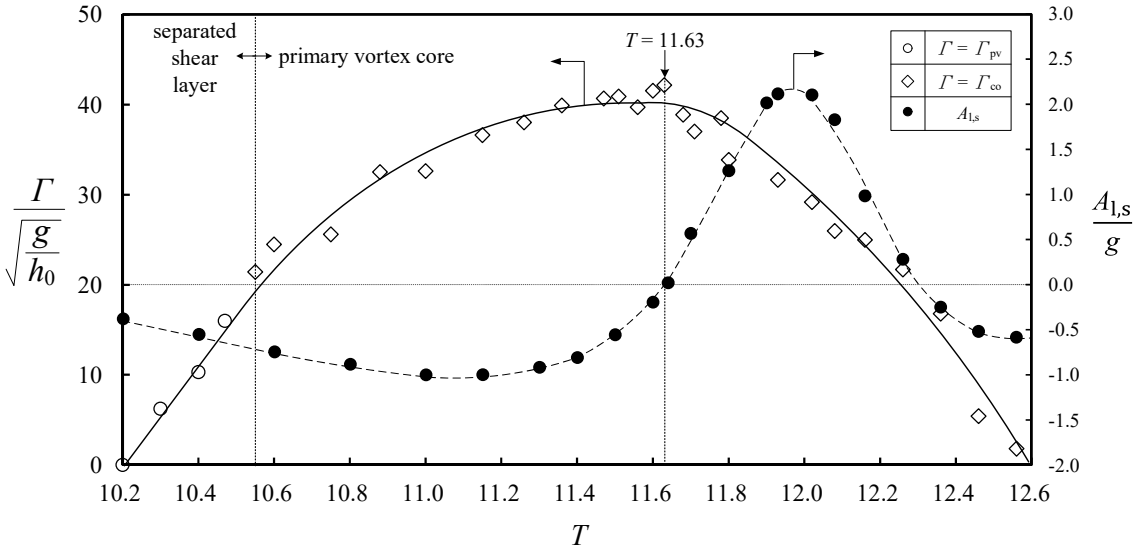

Figure 23. Relationship between the temporal variation in the non-dimensional peak vorticity of the shear layer, $\Gamma_{pv}/[g/h_0]^{1/2}$ or the non-dimensional vorticity of the primary vortex core, $\Gamma_{co}/[g/h_0]^{1/2}$ and the counterpart in the smoothed value of the local acceleration, $A_{l,s}/g$, with respect to the non-dimensional time, T, for 10.20 ≤ T < 12.60.

7. Concluding Remarks

The temporal variations of convection velocity, vorticity, accelerations and pressure gradient in the retreating flow for a non-breaking solitary wave (Case A with H_0/h_0 = 0.363), propagating over a 1:3 sloping beach, have been elucidated experimentally. Flow visualization techniques and HSPIV measurement have been employed to provide qualitative flow images and quantitative velocity data. Some important findings of the flow feature for 10.8 cm ≤ x ≤ 20.2 cm can be drawn as follows:

1. A complete evolution of the solitary wave includes: (a) The wave crest of the solitary wave reaches the toe (located at x = 0) of the sloping bottom for T = 0; (b) Wave propagates over the sloping beach and subsequent run-up motion occurs in absence of wave breaking for 0 < T < 7.25; (c) Wave motion arrives at the maximum run-up height for T = 7.25 at which the first run-up

motion ends; (d) The tip of the wave front stays at a fixed position but with its local free surface profile varying from the bull-nose shape into a sharp-edged one during the very short time interval between $T = 7.25$ and $T = 7.69$. (e) Run-down motion occurs during $7.69 < T < 13.43$; and (f) The second run-up motion starts and evolves for $T \geq 13.43$.

2. The smoothed value of the non-dimensional local acceleration $-A_{l,s}/g$ (i.e., in the offshore direction) for the external stream at $X_{ifs} = 18.81$ cm increases from 0.124 at $T = 7.25$, via 0.377 at $T = 10.20$. With reference to the primary vortex core translating offshore at $T > 10.20$, the value of $-A_{l,s}/g$ at the (moving) core section increases from 0.377 at $T = 10.20$ to a maximum of 0.996 at $T = 11.00$–11.15; and then decreases to zero at about $T = 11.63$, highlighting that the retreating flow is accelerated temporally in the offshore direction. However, for $11.63 \leq T \leq 12.60$, $-A_{l,s}/g$ varies from zero at $T = 11.63$ to a negative maximum of −2.117 at $T = 11.93$ and then changes continuously, via −0.986 at $T = 12.16$, up to zero at about $T = 12.31$, demonstrating the retreating flow decelerated temporally in the offshore direction. It is also interestingly found that $-A_{l,s}/g < -1.0$ for $11.76 < T < 12.16$, strongly indicating the magnitude of the local acceleration unexpectedly larger than the gravity acceleration.
3. The smoothed value of the non-dimensional convective acceleration $-A_{c,s}/g$ (i.e., in the offshore direction) of the external stream at $X_{ifs} = 18.81$ cm ranges from −0.028 at $T = 7.25$ to −0.782 at $T = 10.20$. With respect to the primary vortex core translating offshore, the value of $-A_{c,s}/g$ at the (moving) core section increases from −0.782 at $T = 10.20$ to a negative maximum of −2.005 at $T = 11.15$ (the instant for occurrence of hydraulic jump), then reduces successively up to zero at $T = 11.86$, exhibiting the external stream more decelerated spatially in the offshore direction for $7.25 \leq T \leq 11.86$. Afterwards, $-A_{c,s}/g$ increases continuously from zero up to a positive maximum of 1.013 at $T = 12.08$ and then decreases down to 0.034 at $T = 12.56$, revealing the external stream being accelerated spatially in the offshore direction.
4. For $7.25 \leq T \leq 11.63$, the positive and negative maximum value of $-A_{l,s}/g$ and $-A_{c,s}/g$ in the offshore direction (=0.996 and −2.005) occurs, respectively, at $T = 11.15$. On the other hand, for $11.63 \leq T \leq 12.56$, the negative and positive maximum of $-A_{l,s}/g$ and $-A_{c,s}/g$ (=−2.117 and 1.013) takes place at $T = 11.93$ and 12.08, respectively. Corresponding to the unexpectedly large value of $-A_{l,s}/g = -2.117$ at $T = 11.93$, the partially depth-averaged value of the non-dimensional local acceleration in the vertical direction is equal to $A_{lv,da}/g = 3.37$. The result strongly reconfirms the evident rise of the free surface in the vicinity of $X_{co} = 14.98$ cm for $T = 11.93$ and reveals very rapid change from negative, via nearly zero, to positive vertical velocity for $11.87 \leq T \leq 11.995$ (as shown in Figures 18a and 19b).
5. The smoothed value of the non-dimensional total acceleration $-A_{t,s}/g$ (i.e., in the offshore direction) for the external stream at $X_{ifs} = 18.81$ cm is positive for $7.25 \leq T < 8.30$ but negative for $8.30 \leq T \leq 10.20$ together with $-A_{t,s}/g = 0.091$ at $T = 7.25$, zero at $T = 8.22$ and −0.405 at $T = 10.20$, respectively. Afterwards, with reference to the primary vortex core moving offshore, $-A_{t,s}/g$ decreases consecutively via −1.009 at $T = 11.15$ to a negative maximum of −1.694 at $T = 11.93$; and then increases continuously, via zero at about $T = 12.29$, to 0.615 at $T = 12.56$.
6. The smoothed value of the non-dimensional pressure gradient in the offshore direction at $X_{ifs} = 18.81$ cm increases from $-P^*/g = 0.225$ at $T = 7.25$ to 0.721 at $T = 10.20$, respectively. This trend demonstrates that the external stream of the retreating flow is subjected to increasing adverse pressure gradient and more decelerated spatially with increasing T, thus leading to occurrence of the incipient flow separation at $X_{ifs} = 18.81$ cm for $T = 10.20$. The non-dimensional pressure gradient $-P^*/g$ of the external stream in the offshore direction increases successively from 0.721 at $T = 10.20$, via 1.325 at $T = 11.15$, to a positive maximum of 2.011 at $T = 11.93$ and then to decrease consecutively, via zero at about $T = 12.25$, to −0.299 at $T = 12.56$. Note that $-P^*/g = 2.011$ at $T = 11.93$ demonstrates prominent decelerated flow in the offshore direction under the considerable large adverse pressure gradient, thus further confirming the prominent rise of the free surface in space and sudden increase of the vertical velocity (as shown in Figures 18a and 19b).
7. The non-dimensional peak vorticity in the separated shear layer, $\Gamma_{pv}/[g/h_0]^{1/2}$, increases linearly from zero at $T = 10.20$ to 21.4 at $T = 10.55$. Further, the non-dimensional vorticity of primary

vortex core, $\Gamma_{co}/[g/h_0]^{1/2}$, increases with increasing T for about $10.60 \le T \le 11.63$. The maximum value of the non-dimensional vorticity, $[\Gamma_{co}/(g/h_0)^{1/2}]_{max} = 42.2$, takes place at $T \approx 11.63$. Then $\Gamma_{co}/[g/h_0]^{1/2}$ keeps decreasing with increase in T for $11.63 < T \le 12.56$. Such a feature can be guided to the influence of acceleration ($-A_{l,s} > 0$) and deceleration ($-A_{l,s} < 0$) in the offshore direction for the high-speed external stream within the interval of $10.20 \le T \le 11.63$ and $11.63 \le T \le 12.56$, respectively.

Author Contributions: C.L. was responsible for project administration, technical supervision and quality control of experimental results, with participation from H.-H.H. for partial funding acquisition and discussion. Execution of the investigation, tests, image processing and data analyses were performed by W.-Y.W. The manuscript was written by C.L. Manuscript revisions were done by R.R. and C.-P.T. All the authors contributed to its final version.

Funding: This research was supported by the Ministry of Science and Technology (i.e., the former National Science Council), Taiwan via Grant Nos. MOST 105−221-E−005−033-MY3 and MOST 106−221-E−005−045-MY3 to Department of Civil Engineering, National Chung Hsing University and MOST 105−911-I−006−301 to International Wave Dynamics Research Center, National Cheng Kung University.

Acknowledgments: Special thanks to UTOPIA Instruments Co., Ltd. for helping the installation and testing the high-speed digital camera used.

Conflicts of Interest: The authors declare no conflict of interest.

Appendix A. Details for Calculation of Accelerations

Table A1. A list of velocity data at different times and calculation of the local acceleration A_l with six different time intervals. Note that the partially depth-averaged values of the local acceleration, $A_{l,da}$ and their relative deviations, D_r, are addressed at the bottom of the table

(1)	(2)	(3)	(4)	(5)	(6)	(7)	(8)	(9)	(10)
Y (cm)	$U(X, Y, t - \Delta t)$ (cm/s) t = 0.6455 s	$U(X, Y, t)$ (cm/s) t = 0.6545 s	$U(X, Y, t + \Delta t)$ (cm/s) t = 0.6635 s	A_l (X, Y, t) (cm/s²) Δt = 0.0045 s ΔT = 0.05	A_l (X, Y, t) (cm/s²) Δt = 0.0090 s ΔT = 0.10	A_l (X, Y, t) (cm/s²) Δt = 0.0135 s ΔT = 0.15	A_l (X, Y, t) (cm/s²) Δt = 0.0180 s ΔT = 0.20	A_l (X, Y, t) (cm/s²) Δt = 0.0225 s ΔT = 0.25	A_l (X, Y, t) (cm/s²) Δt = 0.0315 s ΔT = 0.35
0.000	0.00	0.00	0.00						
0.072	−7.25	−8.17	−8.54						
0.132	−14.05	−15.76	−16.48						
0.192	−18.37	−20.89	−20.81						
0.252	−21.57	−24.41	−24.28						
0.312	−23.05	−25.52	−26.31						
0.372	−23.63	−25.74	−27.07						
0.432	−23.82	−25.57	−27.34						
0.492	−23.81	−25.36	−27.30						
0.552	−23.72	−25.18	−27.22	−152.6	−194.0	−153.9	−148.3	−150.3	−138.8
0.612	−23.64	−25.04	−27.14	−162.5	−194.5	−153.5	−147.4	−145.6	−137.1
0.672	−23.56	−24.94	−27.05	−174.3	−194.1	−152.1	−146.7	−141.8	−135.4
0.732	−23.50	−24.89	−26.98	−188.6	−193.0	−149.8	−145.7	−138.5	−134.2
0.792	−23.47	−24.87	−26.89	−202.1	−190.1	−146.9	−144.6	−135.8	−133.9
0.852	−23.46	−24.86	−26.77	−211.0	−184.0	−144.2	−142.4	−132.9	−134.0
0.912	−23.48	−24.86	−26.61	−214.1	−173.9	−141.8	−139.6	−129.8	−134.7
0.972	−23.52	−24.87	−26.41	−211.2	−161.0	−139.5	−136.8	−126.5	−135.4
1.032	−23.56	−24.90	−26.23	−205.3	−148.3	−137.4	−134.4	−123.0	−135.6
1.092	−23.59	−24.96	−26.08	−198.0	−138.1	−135.8	−132.9	−119.5	−135.6
1.152	−23.61	−25.01	−25.98	−191.4	−131.8	−135.1	−132.2	−116.2	−135.2
1.212	−23.62	−25.06	−25.94	−185.1	−128.8	−134.3	−132.3	−113.3	−134.4
1.272	−23.63	−25.09	−25.94	−177.3	−128.1	−132.9	−132.8	−110.9	−133.5
1.332	−23.66	−25.11	−25.97	−170.8	−128.4	−129.9	−133.6	−109.5	−132.4
1.392	−23.70	−25.14	−26.01	−165.7	−128.7	−125.5	−134.1	−108.9	−131.5
1.452	−23.73	−25.16	−26.06	−160.5	−129.4	−121.0	−134.2	−108.9	−130.8
1.512	−23.76	−25.18	−26.10	−156.6	−129.9	−117.3	−133.9	−109.8	−130.3
1.572	−23.78	−25.20	−26.11	−151.1	−129.1	−114.9	−133.2	−110.9	−130.0
1.632	−23.82	−25.22	−26.11	−144.6	−127.4	−113.7	−132.3	−111.9	−129.8
1.692	−23.88	−25.27	−26.12	−137.1	−124.4	−113.0	−130.7	−112.2	−129.7
1.752	−23.95	−25.37	−26.11	−125.9	−120.3	−112.6	−128.6	−111.6	−129.7
1.812	−24.03	−25.49	−26.11	−112.1	−115.8	−112.2	−126.4	−110.2	−129.7
1.872	−24.10	−25.63	−26.11	−96.2	−111.6	−111.8	−124.3	−108.8	−129.8
1.932	−24.16	−25.75	−26.11	−80.6	−108.5	−111.2	−122.6	−107.7	−129.7
1.992	−24.20	−25.85	−26.12	−66.7	−106.7	−110.1	−121.3	−107.1	−129.7
2.052	−24.23	−25.92	−26.13	−54.4	−106.0	−108.4	−120.2	−107.0	−129.7
2.112	−24.25	−25.96	−26.15	−43.7	−105.3	−106.2	−119.6	−107.2	−129.8
2.172	−24.30	−25.98	−26.16	−34.0	−103.6	−104.0	−119.3	−107.5	−130.0
2.232	−24.36	−25.98	−26.18	−25.7	−101.1	−101.7	−118.9	−107.6	−130.3
2.292	−24.43	−25.98	−26.19	−19.1	−97.8	−100.0	−117.9	−107.8	−130.5
2.352	−24.50	−26.01	−26.20	−14.0	−94.5	−98.2	−115.8	−108.2	−130.5
2.412	−24.57	−26.04	−26.21	−9.5	−91.2	−95.9	−113.0	−109.1	−130.4
2.472	−24.63	−26.08	−26.22	−5.2	−87.9	−93.4	−109.8	−110.4	−130.5
2.532	−24.69	−26.11	−26.22	−1.7	−85.1	−90.6	−107.0	−111.9	−130.7
2.592	−24.74	−26.13	−26.23	0.7	−82.9	−88.0	−104.8	−113.3	−131.1
2.652	−24.77	−26.13	−26.24	2.1	−81.3	−85.9	−102.9	−114.6	−132.0
2.712	−24.79	−26.13	−26.24	2.2	−80.4	−84.2	−101.1	−116.3	−133.1
2.772	−24.80	−26.12	−26.24	1.3	−79.8	−83.6	−98.9	−117.9	−134.1
2.832	−24.81	−26.11	−26.24	−0.4	−79.5	−83.9	−96.3	−119.4	−135.4
2.892	−24.80	−26.10	−26.23	−2.7	−79.4	−84.4	−94.9	−120.2	−136.3
2.952	−24.79	−26.08	−26.22	−5.2	−79.6	−88.4	−92.7	−120.2	−136.8
3.012	−24.79	−26.06	−26.21	−7.9	−79.3	−89.2	−93.0	−118.3	−137.0
3.072	−24.79	−26.03	−26.21	−9.2	−79.1	−89.2	−93.0	−117.6	−136.7
3.132	−24.79	−26.02	−26.21	−8.1	−79.0	−89.2	−93.0	−116.6	−136.4
3.192	−24.79	−26.01	−26.20	−3.9	−78.8	−89.2	−93.0	−116.5	−135.9
3.252	−24.79	−26.01	−26.21	−0.9	−79.2	−89.2	−93.0	−116.5	−134.4
3.312	−24.79	−26.01	−26.21	8.5	−78.8	−89.2	−93.0	−116.5	−134.0
3.372	−24.79	−26.01	−26.17	29.3	−76.6	−89.2	−93.0	−116.5	
3.432	−24.79								
						$A_{l,da}$ (X, t) (cm/s²)			
				−88.4	−116.8	−111.9	−119.9	−117.1	−132.9
	expected average estimated from the values of $A_{l,da}$ for Δt = 0.0090, 0.0135, 0.0180 and 0.0225 s					relative deviation D_r (%)			
	−116.4 (cm/s²)			24.1	0.3	3.9	3.0	0.6	14.2

Table A2. A list of velocity data obtained at different sections for T = 7.25 and calculation of the first convective acceleration A_{c1} with seven distinct spatial intervals, together with the partially depth-averaged values of the first convective acceleration, $A_{c1,da}$ and their relative deviations, D_r, presented at the bottom of table

(1)	(2)	(3)	(4)	(5)	(6)	(7)	(8)	(9)	(10)	(11)
Y (cm)	$U(X-\Delta X, Y, t)$ (cm/s) X = 17.85 cm	$U(X, Y, t)$ (cm/s) X = 18.81 cm	$U(X+\Delta X, Y, t)$ (cm/s) X = 19.77 cm	$A_{c1}(X, Y, t)$ (cm/s²) ΔX = 0.24 cm	$A_{c1}(X, Y, t)$ (cm/s²) ΔX = 0.42 cm	$A_{c1}(X, Y, t)$ (cm/s²) ΔX = 0.60 cm	$A_{c1}(X, Y, t)$ (cm/s²) ΔX = 0.78 cm	$A_{c1}(X, Y, t)$ (cm/s²) ΔX = 0.96 cm	$A_{c1}(X, Y, t)$ (cm/s²) ΔX = 1.02 cm	$A_{c1}(X, Y, t)$ (cm/s²) ΔX = 1.38 cm
0.000	0.00	0.00	0.00							
0.072	−8.55	−8.17	−8.20							
0.132	−14.94	−15.76	−16.92							
0.192	−19.65	−20.89	−22.36							
0.252	−22.53	−24.41	−26.25							
0.312	−23.45	−25.52	−27.32							
0.372	−23.54	−25.74	−27.53							
0.432	−23.26	−25.57	−27.42							
0.492	−22.95	−25.36	−27.29							
0.552	−22.71	−25.18	−27.11	98.6	73.8	67.9	59.3	57.7	57.2	55.8
0.612	−22.55	−25.04	−26.92	100.3	76.3	72.5	59.8	57.0	56.3	54.3
0.672	−22.48	−24.94	−26.73	96.6	77.8	75.0	59.1	55.3	55.0	52.8
0.732	−22.45	−24.89	−26.60	89.0	78.2	74.4	58.1	53.8	53.5	51.4
0.792	−22.43	−24.87	−26.50	78.8	77.6	71.1	56.8	52.7	52.2	50.0
0.852	−22.41	−24.86	−26.45	67.3	75.2	66.2	55.7	52.3	50.8	48.6
0.912	−22.41	−24.86	−26.42	54.7	70.2	60.9	55.0	51.9	49.2	46.9
0.972	−22.48	−24.87	−26.45	42.7	62.6	55.3	53.9	51.4	47.7	45.1
1.032	−22.63	−24.90	−26.52	33.7	52.6	49.1	52.0	50.4	46.4	43.3
1.092	−22.84	−24.96	−26.61	29.7	42.1	42.2	48.5	49.1	45.4	41.7
1.152	−23.06	−25.01	−26.67	30.6	33.2	35.7	43.4	47.0	44.6	40.5
1.212	−23.26	−25.06	−26.66	33.2	27.5	31.4	38.0	44.3	43.8	39.8
1.272	−23.43	−25.09	−26.57	34.2	25.3	30.0	33.3	40.9	42.8	39.3
1.332	−23.59	−25.11	−26.45	31.9	24.9	30.8	30.2	37.4	41.2	38.7
1.392	−23.74	−25.14	−26.31	27.5	25.3	31.9	28.1	33.6	38.6	37.8
1.452	−23.92	−25.16	−26.18	23.5	25.3	31.4	26.0	29.6	35.0	36.5
1.512	−24.09	−25.18	−26.03	22.2	25.7	29.2	23.0	25.5	30.9	34.7
1.572	−24.25	−25.20	−25.90	23.1	26.9	26.1	19.3	21.7	27.1	32.2
1.632	−24.35	−25.22	−25.80	24.6	29.3	23.1	15.6	19.0	24.5	29.6
1.692	−24.43	−25.27	−25.77	24.7	31.2	20.9	12.7	17.6	23.0	27.0
1.752	−24.50	−25.37	−25.81	22.6	31.4	19.6	11.1	17.3	22.2	24.9
1.812	−24.60	−25.49	−25.90	18.7	29.2	18.8	10.7	17.2	21.4	23.6
1.872	−24.74	−25.63	−26.01	13.2	25.3	18.0	11.1	17.0	20.4	23.0
1.932	−24.90	−25.75	−26.12	6.7	20.9	17.1	11.8	16.4	19.3	23.1
1.992	−25.06	−25.85	−26.21	0.5	16.7	15.7	12.2	15.5	18.1	23.5
2.052	−25.18	−25.92	−26.27	−4.7	12.8	14.3	12.3	14.7	16.7	23.6
2.112	−25.27	−25.96	−26.29	−7.1	9.9	13.3	12.1	13.7	15.2	23.2
2.172	−25.32	−25.98	−26.28	−6.9	8.0	13.2	11.6	13.0	13.4	22.1
2.232	−25.36	−25.98	−26.26	−4.8	7.7	13.3	11.0	12.1	11.6	20.6
2.292	−25.41	−25.98	−26.24	−2.2	8.2	12.9	10.5	11.3	10.1	18.9
2.352	−25.48	−26.01	−26.24	−0.4	8.4	11.4	10.0	10.3	8.9	17.4
2.412	−25.57	−26.04	−26.25	0.7	8.0	9.1	9.5	9.2	8.1	16.2
2.472	−25.67	−26.08	−26.28	1.1	6.6	6.6	8.8	8.3	7.5	15.4
2.532	−25.74	−26.11	−26.29	1.2	5.1	4.8	8.0	7.5	6.9	15.0
2.592	−25.78	−26.13	−26.30	1.2	3.6	4.0	7.4	7.1	6.4	14.9
2.652	−25.79	−26.13	−26.29	1.3	3.0	4.1	7.3	6.9	6.2	14.8
2.712	−25.78	−26.13	−26.28	1.7	3.0	4.8	7.9	6.9	6.3	14.6
2.772	−25.75	−26.12	−26.28	2.5	3.8	5.9	9.3	7.2	7.0	14.5
2.832	−25.71	−26.11	−26.28	3.2	4.6	6.9	11.0	7.7	8.0	14.4
2.892	−25.66	−26.10	−26.28	3.8	5.0	7.6	12.8	8.5	8.9	14.0
2.952	−25.59	−26.08	−26.28	3.7	4.6	8.0	14.1	9.4	9.8	14.2
3.012	−25.50	−26.06	−26.26	2.7	3.4	7.8	14.1	10.3	10.4	14.8
3.072	−25.42	−26.03	−26.22	0.4	1.1	7.3	13.6	10.8	11.0	
3.132	−25.37	−26.02	−26.17	−1.8	−2.4	5.9	12.1	10.8	11.3	
3.192	−25.38	−26.01	−26.09	−2.2	−7.8	4.1	10.1	9.7		
3.252	−25.45	−26.01		−0.9	−12.0	1.7	8.9			
3.312	−25.53	−26.01		2.7	−15.5					
3.372	−25.57	−26.01								
3.432	−25.49									
							$A_{c1,da}(X, t)$ (cm/s²)			
				21.8	24.5	25.7	24.1	25.0	26.1	29.8
	expected average estimated from the values of $A_{c1,da}$ for ΔX = 0.42, 0.60, 0.78, 0.96 and 1.02 cm						relative deviation D_r (%)			
	25.1 (cm/s²)			13.1	2.4	2.4	4.0	0.4	4.0	18.7

Table A3. A list of velocity data for $T = 7.25$ and calculation of A_{c2} and A_c (=$A_{c1} + A_{c2}$), A_t and $(1/\varrho)\partial P/\partial X$. Note that partially depth-averaged values for $A_{c2,da}$, $A_{c,da}$, $A_{t,da}$ and $[(1/\varrho)\partial P/\partial X]_{da}$ are all shown at the bottom of the table.

(1)	(2)	(3)	(4)	(5)	(6)	(7)
Y (cm)	$V(X, Y, t)$ (cm/s)	$U(X, Y, t)$ (cm/s)	A_{c2} (X, Y, t) (cm/s²)	A_c (X, Y, t) (cm/s²)	A_t (X, Y, t) (cm/s²)	$(1/\varrho)\partial P/\partial X$ (cm/s²)
0.000	0.00	0.00				
0.072	0.07	−8.17				
0.132	0.11	−15.76				
0.192	0.16	−20.89				
0.252	0.30	−24.41				
0.312	0.54	−25.52				
0.372	0.86	−25.74				
0.432	1.20	−25.57				
0.492	1.46	−25.36				
0.552	1.63	−25.18	3.5	61.3	−132.7	−177.5
0.612	1.73	−25.04	2.4	59.3	−135.1	−175.1
0.672	1.81	−24.94	1.2	56.5	−137.6	−172.7
0.732	1.90	−24.89	0.1	53.9	−139.1	−171.1
0.792	2.02	−24.87	−0.6	52.2	−138.0	−172.3
0.852	2.14	−24.86	−0.5	51.8	−132.1	−178.1
0.912	2.29	−24.86	0.3	52.1	−121.8	−188.5
0.972	2.46	−24.87	1.2	52.6	−108.4	−201.8
1.032	2.64	−24.90	1.8	52.2	−96.1	−214.1
1.092	2.82	−24.96	1.7	50.7	−87.4	−222.8
1.152	2.98	−25.01	0.9	47.9	−83.9	−226.3
1.212	3.11	−25.06	−0.3	44.0	−84.8	−225.4
1.272	3.21	−25.09	−1.4	39.5	−88.6	−221.6
1.332	3.26	−25.11	−2.0	35.3	−93.0	−217.2
1.392	3.28	−25.14	−2.0	31.6	−97.1	−213.2
1.452	3.28	−25.16	−1.5	28.1	−101.4	−208.9
1.512	3.28	−25.18	−1.1	24.4	−105.5	−204.7
1.572	3.29	−25.20	−1.7	20.0	−109.1	−201.1
1.632	3.31	−25.22	−3.5	15.6	−111.9	−198.4
1.692	3.34	−25.27	−6.0	11.6	−112.8	−197.4
1.752	3.36	−25.37	−8.0	9.3	−111.0	−199.2
1.812	3.37	−25.49	−8.4	8.9	−106.9	−203.3
1.872	3.38	−25.63	−7.3	9.7	−102.0	−208.2
1.932	3.38	−25.75	−5.3	11.1	−97.4	−212.8
1.992	3.37	−25.85	−3.5	12.1	−94.6	−215.6
2.052	3.35	−25.92	−2.0	12.6	−93.3	−216.9
2.112	3.34	−25.96	−0.9	12.8	−92.4	−217.8
2.172	3.32	−25.98	−0.2	12.8	−90.8	−219.4
2.232	3.31	−25.98	0.2	12.3	−88.8	−221.4
2.292	3.29	−25.98	−0.1	11.2	−86.7	−223.6
2.352	3.28	−26.01	−0.7	9.6	−84.9	−225.3
2.412	3.28	−26.04	−1.1	8.1	−83.1	−227.1
2.472	3.28	−26.08	−1.2	7.0	−80.9	−229.3
2.532	3.28	−26.11	−0.9	6.6	−78.5	−231.7
2.592	3.28	−26.13	−0.5	6.6	−76.3	−233.9
2.652	3.29	−26.13	−0.2	6.7	−74.6	−235.6
2.712	3.29	−26.13	0.0	6.9	−73.5	−236.7
2.772	3.30	−26.12	0.0	7.2	−72.6	−237.6
2.832	3.29	−26.11	0.0	7.7	−71.8	−238.4
2.892	3.29	−26.10	0.0	8.5	−70.9	−239.3
2.952	3.29	−26.08	−0.1	9.3	−70.3	−239.9
3.012	3.30	−26.06	−0.3	10.0	−69.3	−240.9
3.072	3.32	−26.03	−0.8	10.1	−69.0	−241.2
3.132	3.37	−26.02	−1.3	9.5	−69.4	−240.8
3.192	3.45	−26.01	−2.0	7.7	−71.0	−239.2
3.252	3.54	−26.01	−2.5			
3.312	3.65	−26.01	−2.5			
3.372	3.73	−26.01				
			$A_{c2,da}$ (X, t) (cm/s²)	$A_{c,da}$ (X, t) (cm/s²)	$A_{t\,da}$ (X, t) (cm/s²)	$[(1/\varrho)\partial P/\partial X]_{da}$ (cm/s²)
			−1.2	23.8	−95.5	−214.7

Table A4. Nomenclature.

Term	Definition
$[(1/\varrho)\partial P/\partial X]_{da}$	partially depth-averaged value of pressure gradient divided by density [LT⁻²]
$A_{c,s}$	smoothed value of convective acceleration [LT⁻²]
A_{c1}	(=$U\partial U/\partial X$) first convective acceleration [LT⁻²]
$A_{c1,da}$	(=$(U\partial U/\partial X)_{da}$) partially depth-averaged value of first convective acceleration [LT⁻²]
$A_{c1,s}$	smoothed value of first convective acceleration [LT⁻²]
A_{c2}	(=$V\partial U/\partial Y$) second convective acceleration [LT⁻²]
$A_{c2,da}$	(=$(V\partial U/\partial Y)_{da}$) partially depth-averaged value of second convective acceleration [LT⁻²]
$A_{c2,s}$	smoothed value of second convective acceleration [LT⁻²]
A_l	(=$\partial U/\partial t$) local acceleration [LT⁻²]
$A_{l,da}$	(=$(\partial U/\partial t)_{da}$) depth-averaged value of local acceleration [LT⁻²]
$A_{l,s}$	smoothed value of local acceleration [LT⁻²]
$A_{lv,da}$	(=$(\partial V/\partial t)_{da}$) partially depth-averaged value of local acceleration in Y-direction [LT⁻²]

A_t	(=$A_l + A_{c1} + A_{c2}$) total acceleration [LT^{-2}]
$A_{t,da}$	(=$(A_l + A_{c1} + A_{c2})_{da}$) partially depth-averaged value of total acceleration [LT^{-2}]
$A_{t,s}$	smoothed value of total acceleration [LT^{-2}]
C^*	(=$(gh_0)^{1/2}$) linear wave celerity [LT^{-1}]
C_0	measured wave celerity over horizontal bottom [LT^{-1}]
D_r	relative deviation [-]
g	gravity acceleration [LT^{-2}]
H_0	incident wave height [L]
H_p	potential associated with gravitational force [-]
h_0	still water depth [L]
l_s	representative length scale [L]
P	pressure [$ML^{-1}T^{-2}$]
P^*	(=$[(1/\varrho)\partial P/\partial X]_s$) smoothed value of pressure gradient divided by density [LT^{-2}]
S^*	(=$1.521 \times S_0 \times (H_0/h_0)^{-1/2}$) slope parameter [-]
S_0	slope of sloping beach [-]
T	(=$t \times (g/h_0)^{1/2}$) non-dimensional time [-]
T_{hj}	non-dimensional time for occurrence of hydraulic jump [-]
T_{ifs}	non-dimensional time for incipient flow separation [-]
T_{mrh}	non-dimensional time for wave tip reaching maximum run-up height [-]
t	time defining relative position of wave crest from toe of sloping beach [T]
t_{hj}	time for occurrence of hydraulic jump [T]
t_{ifs}	time for incipient flow separation [T]
t_{mrh}	time for wave tip reaching maximum run-up height [T]
t_p	period of solitary wave [T]
U	ensemble-averaged velocity parallel to sloping beach [LT^{-1}]
U_{cv}	convection velocity of primary vortex core [LT^{-1}]
U_r	representative velocity parallel to sloping beach [LT^{-1}]
U_u	uniform or partially-depth-averaged velocity parallel to sloping beach [LT^{-1}]
u	ensemble-averaged horizontal velocity [LT^{-1}]
u_{max}	maximum value of ensemble-averaged horizontal velocity in time history [LT^{-1}]
u_s	representative velocity scale [LT^{-1}]
v	ensemble-averaged vertical velocity [LT^{-1}]
V	ensemble-averaged velocity normal to sloping beach [LT^{-1}]
X	onshore distance parallel to sloping beach with $X = 0$ located at toe of sloping beach [L]
X_{co}	position in X-direction where primary vortex core is located [L]
X_{ifs}	position in X-direction where incipient flow separation occurs [L]
X_{pv}	position in X-direction where peak vorticity occurs [L]
x	horizontal onshore distance with $x = 0$ located at toe of sloping beach [L]
x_{hj}	position in x-direction where hydraulic jump occurs [L]
x_{ifs}	position in x-direction where incipient flow separation occurs [L]
x_{mrh}	position in x-direction where wave-tip reaches maximum run-up height [L]
Y	height perpendicular to sloping beach with $Y = 0$ located at the slope surface [L]
Y_{co}	position in Y-direction where primary vortex core is located [L]
Y_{pv}	position in Y-direction where peak vorticity occurs [L]
Y_{size}	height corresponding to size of primary vortex in Y-direction [L]
y	vertical upward distance measured from horizontal bottom [L]
Δt	time interval [T]
$\Delta t_{framing}$	time elapse between two consecutive images taken by high-speed camera at specified framing rate [T]
ΔX	spatial interval [L]
ϱ	fluid density [ML^{-3}]
μ	dynamic viscosity [$ML^{-1}T^{-1}$]
τ	shear stress [$ML^{-1}T^{-2}$]
η	free surface elevation over sloping beach [L]
η_0	free surface elevation over horizontal bottom [L]
θ	inclination angle of sloping beach [-]
Γ	vorticity [T^{-1}]
Γ_{co}	vorticity at primary vortex core [T^{-1}]

Γ_{pv}	peak vorticity [T^{-1}]
$(\ldots)_A$	physical quantity of Case A
$(\ldots)_B$	physical quantity of Case B

References

1. Lin, C.; Wong, W.Y.; Kao, M.J.; Tsai, C.P.; Hwung, H.H.; Wu, Y.T.; Raikar, R.V. Evolution of velocity field and vortex structure during run-down of solitary wave over very steep beach. *Water* **2018**, *10*, 1713.
2. Carrier, G.F.; Greenspan, H.P. Water waves of finite amplitude on a sloping beach. *J. Fluid Mech.* **1958**, *17*, 97–110.
3. Synolakis, C.E. The runup of solitary waves. *J. Fluid Mech.* **1987**, *185*, 523–545.
4. Kobayashi, N.; Otta, A.K.; Roy, I. Wave reflection and runup on rough slopes. *J. Waterw. Port Coast. Ocean Eng.* **1987**, *113*, 282–298.
5. Zelt, J.A. The run-up of nonbreaking and breaking solitary waves. *Coast. Eng.* **1991**, *15*, 205–246.
6. Grilli, S.T.; Subramanya, R.; Svendsen, I.A.; Veeramony, J. Shoaling of solitary waves on plane beaches. *J. Waterw. Port Coast. Ocean Eng.* **1994**, *120*, 609–628.
7. Grilli, S.T.; Svendsen, I.A.; Subramanya, R. Breaking criterion and characteristics for solitary waves on slopes. *J. Waterw. Port Coast. Ocean Eng.* **1997**, *123*, 102–112.
8. Lin, P.; Liu, P.L.F. A numerical study of breaking waves in the surf zone. *J. Fluid Mech.* **1998**, *359*, 239–264.
9. Lin, P.; Chang, K.A.; Liu, P.L.F. Runup and rundown of solitary waves on sloping beaches. *J. Waterw. Port Coast. Ocean Eng.* **1999**, *125*, 247–255.
10. Scandura, P.; Foti, E.; Faraci, C. Mass transport under standing waves over a sloping beach. *J. Fluid Mech.* **2012**, *701*, 460–472.
11. Higuera, P.; Liu, P.L.F.; Lin, C.; Wong, W.Y.; Kao, M.J. Laboratory-scale swash flows generated by a non-breaking solitary wave on a steep slope. *J. Fluid Mech.* **2018**, *847*, 186–227.
12. Jensen, A.; Pedersen, G.K.; Wood, D.J. An experimental study of wave run-up at a steep beach. *J. Fluid Mech.* **2003**, *486*, 161–188.
13. Pedersen, G.; Lindstrom, E.; Bertelsen, A.F.; Jensen, A.; Laskovski, D. Runup and boundary layers on sloping beaches. *Phys. Fluids* **2013**, *25*, 012102.
14. Lin, C.; Yeh, P.H.; Hseih, S.C.; Shih, Y.N.; Lo, L.F.; Tsai, C.P. Pre-breaking internal velocity field induced by a solitary wave propagating over a 1:10 slope. *Ocean Eng.* **2014**, *80*, 1–12.
15. Lin, C.; Kao, M.J.; Tzeng, G.W.; Wong, W.Y.; Yang, J.; Raikar, R.V.; Wu, T.R.; Liu, P.L.F. Study on flow fields of boundary-layer separation and hydraulic jump during rundown motion of shoaling solitary wave. *J. Earthq. Tsunami* **2015**, *9*, 154002.
16. Smith, L.; Jensen, A.; Pedersen, G. Investigation of breaking and non-breaking solitary waves and measurements of swash zone dynamics on a 5° beach. *Coast. Eng.* **2017**, *120*, 38–46.
17. Petrotta, C.; Faraci, C.; Scandura, P.; Foti, E. Experimental investigation on sea ripple evolution over sloping beaches. *Ocean Dyn.* **2018**, *68*, 1221–1237.
18. Chang, K.A.; Liu, P.L.F. Velocity, acceleration and vorticity under a breaking wave. *Phys. Fluids* **1998**, *10*, 327–329.
19. Jensen, A.; Sveen, J.K.; Grue, J.; Richon, J.B.; Gray, C. Acceleration in water waves by extended particle image velocimetry. *Exp. Fluids* **2001**, *30*, 500–510.
20. Puleo, J.A.; Farhadzadeh, A.; Kobayashi, N. Numerical simulation of swash zone fluid accelerations. *J. Geophys. Res.* **2007**, *112*, C07007.
21. Pedrozo-Acuna, A.; Alegria-Arzaburu, A.R.; Torres-Freyermuth, A.; Mendoza, E.; Silva, R. Laboratory investigation of pressure gradients induced by plunging breakers. *Coast. Eng.* **2011**, *58*, 722–738.
22. Goring, D.G. *Tsunami: The Propagation of Long Waves onto a Shelf*; Technical Report No. KH-R–38; W. M. Keck Laboratory of Hydraulics and Water Resources, California Institute of Technology: Pasadena, CA, USA, 1978.
23. Dean, R.G.; Dalrymple, R.A. *Water Wave Mechanics for Engineers and Scientists*; World Scientific Publishing Co. Pte. Ltd.: Hackensack, NJ, USA, 1995.
24. Ho, T.C. Characteristics of Vortical Flow Fields Induced by Solitary Waves Propagating over Submerged Structures with Different Aspect Ratios. Ph. D. Thesis, Department of Civil Engineering, National Chung Hsing University, Taichung, Taiwan, 2009.

25. Chow, V.T. *Open-Channel Hydraulics*; McGraw-Hill Book Company: Singapore, Singapore, 1973; pp. 425–428.
26. Subramanya, K. *Flow in Open Channels*; McGraw-Hill Book Company: New York, NY, USA, 1986; pp. 204–206.
27. Sumer, B.M.; Sen, M.B.; Karagali, I.; Ceren, B.; Fredsøe, J.; Sottile, M.; Zilioli, L.; Fuhrman, D.R. Flow and sediment transport induced by a plunging solitary wave. *J. Geophys. Res.* **2011**, *116*, C01008, doi:10.1029/2010JC006435.
28. Daily, J.W.; Harleman, D.R.F. *Fluid Dynamics*; Addison-Wesley Publishing Company, Inc.: Boston, MA, USA, 1966.
29. Munson, B.R.; Young, D.F.; Okiishi, T.H. *Fundamentals of Fluid Mechanics*; John Wiley & Sons, Inc.: Hoboken, NJ, USA, 1990.
30. Liu, P.L.F.; Park, Y.S.; Cowen, E.A. Boundary layer flow and bed shear stress under a solitary wave. *J. Fluid Mech.* **2007**, *574*, 449–463.
31. Sumer, B.M.; Jensen, P.M.; Sørensen, L.B.; Fredsøe, J.; Liu, P.L.F.; Carstensen, S. Coherent structures in wave boundary layers. Part 2. Solitary motion. *J. Fluid Mech.* **2010**, *646*, 207–231.
32. Lin, C.; Yu, S.M.; Wong, W.Y.; Tzeng, G.W.; Kao, M.J.; Yeh, P.H.; Raikar, R.V.; Yang, J.; Tsai, C.P. Velocity characteristics in boundary layer flow caused by solitary wave traveling over horizontal bottom. *Exp. Therm. Fluid Sci.* **2016**, *76*, 238–252.
33. Baldock, T.E.; Grayson, R.; Torr, B.; Power, H.E. Flow convergence at the tip of a viscous swash front—Experimental and analytical modeling, *Coast. Eng.* **2014**, *88*, 123–130.
34. Nielsen, P. Bed shear stress, surface shape and velocity field near the tip of dam-breaks, tsunami and wave runup, *Coast. Eng.* **2018**, *138*, 126–131.
35. Park, Y.S.; Liu, P.L.F.; Chen, I.C. Contact line dynamics and boundary layer flow during reflection of a solitary wave, *J. Fluid Mech.* **2012**, *707*, 307–330.
36. Henderson, F.M. *Open Channel Flow*; Macmillan Publishing Company Inc.: New York, NY, USA, 1966; pp. 218–219.
37. Schlichting, H. *Boundary Layer Theory*; McGraw-Hill Book Company: New York, NY, USA, 1979.
38. Lin, C.; Hsieh, S.C.; Lin, W.J.; Raikar, V.R. Characteristics of recirculation zone structure behind an impulsively started circular cylinder. *J. Eng. Mech.* **2012**, *138*, 184–198.